minerals

MDPI

Article

Developing Characteristics of Shale Lamination and Their Impact on Reservoir Properties in the Deep Wufeng–Longmaxi Formation Shale of the Southern Sichuan Basin

Xiao Ma [1,2,3], Jinqi Xu [3], Wenhui Liu [3], Yaohua Wang [3], Huricha Wu [3] and Jingqiang Tan [1,2,3,*]

[1] Key Laboratory of Metallogenic Prediction of Nonferrous Metal and Geological Environment Monitoring (Central South University), Ministry of Education, Changsha 410083, China; mx1992cq@163.com
[2] Key Laboratory of Non-Ferrous and Geological Hazard Detection, Changsha 410083, China
[3] School of Geosciences and Info-Physics, Central South University, Changsha 410083, China; jinqixu2001@163.com (J.X.); liuwenhui_98@163.com (W.L.); 225001040@csu.edu.cn (Y.W.); 215012114@csu.edu.cn (H.W.)
* Correspondence: tanjingqiang@csu.edu.cn; Tel.: +86-186-7486-8510

Abstract: The deep shale of the Wufeng–Longmaxi Formation in the southern Sichuan Basin has high gas potential. The development characteristics of lamination could significantly impact reservoir property. Samples were investigated using microscopic observation, element analysis, organic petrology analysis, mineralogy analysis, and pore structure analysis to determine the types of laminae and laminasets, clarify the formation conditions of argillaceous lamina and silty lamina as well as their relationships with the sedimentary environment, and explore the influence of laminae on shale reservoir property. Results indicate that the Wufeng Formation shale exhibits weak development of laminae due to bioturbation, while the Longmaxi Formation shale develops continuous, parallel, and plate-like laminae. Compared with light silty lamina-rich shale, dark argillaceous lamina-rich shale usually develops in an anoxic reduction environment, with higher total organic carbon content, porosity, pore volume, specific surface area, and more developed organic matter pores, which can provide greater space for shale gas adsorption and storage. Shales in the middle section of the Longmaxi Formation are characterized by the development of silty-argillaceous interbedded type laminaset, which have good reservoir performance, making them the primary target for deep shale gas exploration and development.

Keywords: sedimentary environment; lamina; pore structure; Sichuan basin; Wufeng–Longmaxi Formation

check for updates

Citation: Ma, X.; Xu, J.; Liu, W.; Wang, Y.; Wu, H.; Tan, J. Developing Characteristics of Shale Lamination and Their Impact on Reservoir Properties in the Deep Wufeng–Longmaxi Formation Shale of the Southern Sichuan Basin. *Minerals* **2024**, *14*, 171. https://doi.org/10.3390/min14020171

Academic Editors: Roberto Buccione and Rabah Kechiched

Received: 7 January 2024
Revised: 31 January 2024
Accepted: 1 February 2024
Published: 4 February 2024

1. Introduction

The marine shale formations in the Sichuan Basin, specifically from the Upper Ordovician Wufeng Formation to the Lower Silurian Longmaxi Formation, are known for their significant thickness and stability. In the early stage of resource investigation and evaluation, researchers primarily focused on shale formations with burial depths of less than 3500 m, leading to the development of various theories and technologies for mid-shallow marine shale gas exploration and development [1–6]. In recent years, with the continuous advancements in both theoretical understanding and technological capabilities, there has been a notable shift in focus towards the exploration and development of deep (burial depth >3500–4500 m) and ultradeep (burial depth >4500 m) shale gas in the southwestern margin of the Sichuan Basin [7]. Compared to mid-shallow shale formations at depths of 2000–3500 m, deep shale reservoirs exhibit more complex geological structures and possess unique characteristics, including high formation pressure and high-pressure coefficients [8]. More efforts are needed to conduct systematic research on the depositional characteristics and reservoir quality.

During the sedimentation process, there exists a complex geochemical equilibrium between the sediment and the depositional environment. By utilizing elemental geochemical indicators and combining them with characteristics such as minerals in the rocks and sedimentary structures, it is possible to reveal the changing characteristics of shale depositional environments [9,10]. Reservoir property characterization is the core of evaluating hydrocarbon source rock reservoirs and serves as the foundation for studying the enrichment mechanisms of shale oil and gas [11]. Shale reservoirs have developed abundant nanoscale pores and microfractures, which play a crucial role in gas adsorption and storage, resulting in complex pore structures and increased heterogeneity [12–14]. Based on the study of pore types in the Barnett Shale and Woodford Shale, Slatt and O'Brien divided pore types into six categories [15], which were subsequently simplified into three categories: intergranular pores, intragranular pores, and organic matter pores [16]. The International Union of Pure and Applied Chemistry (IUPAC) classifies pores into micropores (pore size <2 nm), mesopores (pore size ranging from 2 to 50 nm), and macropores (pore size >50 nm) based on pore size [17]. Currently, shale pore characterization techniques are primarily divided into qualitative observation and quantitative testing, and more details can be found in Wang et al. [18]. Qualitative observation is mainly achieved through radiation detection techniques, with FE-SEM being the most commonly used technique for observing shale pores [19]. Quantitative tests mainly include nuclear magnetic resonance (NMR), nanoscale computed tomography (CT) scan, small and ultra small angle neutron scattering (SANS/USANS), and fluid injection techniques, such as gas adsorption or mercury injection (MICP) [20–22]. In recent years, researchers studying shale pore structure characterization have adopted a combined approach using multiple methods to obtain more refined information [23]. However, research on the relationship between pore structure, sedimentary environment, and lamina characteristics is still relatively scare [24].

Laminae refer to the smallest macroscopically recognizable layers in a sedimentary sequence that lack internal stratification. In recent years, an increasing number of scholars have realized that laminae not only reflect the sedimentary characteristics of shale but also contain information related to reservoir performance and shale gas enrichment, making it an essential aspect of the fundamental research, exploration and development of unconventional oil and gas [25,26]. It is important to focus on the morphology, continuity, and geometric relationships of the laminae in fine-grained sedimentary deposits (with particle sizes less than 0.00625 mm), as well as to consider the mineral composition, grain size variations, and interface contacts [27]. Shi et al. [28] proposed that studies of lamination should first identify and distinguish individual laminae, laminasets, and beds and then extract their composition, texture, and structure as key attributes to characterize their developmental characteristics. Methods such as visual and microscopic observation and software quantification can be utilized to determine these attributes. The key attributes of lamina composition are organic matter and mineral content [29], which are mainly influenced by the interaction of physical, chemical, and biological processes during deposition and diagenesis [30]. The main parameter of lamina texture is particle size, while main parameters of lamina structure include the morphology, continuity, and superposition relationships. They can be used to reconstruct sediment sources and paleoenvironments, as well as to determine changes in water flow direction and energy [24,31].

To clarify the depositional environment, lamina development, and pore structure characteristics of the deep Wufeng–Longmaxi shale in the southern part of the Sichuan Basin, we selected laminated, organic-rich shales from Well L in the Luzhou area and Well Y in the Tiangongtang area as the research objects. Shallow shales from Well N in the Changning area were used as a reference. Geological features such as the paleoclimate, paleoredox conditions, and paleowater dynamic conditions during the sedimentary period were reconstructed by elemental analysis techniques. Systematic identification and classification of lamina and laminasets were conducted from a macroscopic and microscopic scale to reveal the development characteristics and formation mechanisms of the laminae. Fine characterization of shale pore structure is conducted by MICP and gas adsorption to discuss reservoir property. By revealing the matching relationship among the sedimentary environment, lamina development characteristics, and reservoir properties, we aim to provide theoretical support for the exploration and development of deep shale gas in the Sichuan Basin and offer a reference for the development of the geological theory of marine shale gas.

2. Geological Background

The Sichuan Basin is located in the northwestern part of the Yangtze Platform, with a rhomboid-shaped distribution in NE–SW [32]. It is delineated by large-scale folds and faults, including the Dabashan thrust-fold belt, Longmen Shan thrust-fold belt, and Emeishan fault zone (Figure 1a). The Sichuan Basin is a superposed basin that has undergone multiple episodes of tectonic evolution. During the late Ordovician, the Katian Stage deposited black shale from the Wufeng Formation. In the early Silurian period, global temperatures decreased, and sea levels dropped [33]. During the Hirnantian Stage, sea levels rapidly decreased, leading to the rapid and widespread exposure of the Kangdian Old Land and Qianzhong Old Land. In some areas within the basin, sedimentary layers are dominated by lithologies such as shell limestone, known as the Guanyinqiao Member. In the early Rhuddanian period, the global climate warmed and glacial melting occurred, leading to a large-scale marine transgression in the entire region. The depositional water bodies deepened further, resulting in the deposition of carbon-rich and silica-rich black shale at the base of the Longmaxi Formation. The material sources of siliceous minerals such as quartz are mainly terrestrial debris and biogenic siliceous materials. The input of terrestrial debris is controlled by factors such as water depth and source distance. Biogenic silica mainly originates from biogenic siliceous skeletons and crustacean organisms. Clay minerals mainly originate from the input of terrestrial debris. Carbonate minerals are mostly derived from biogenic precipitation and chemical precipitation, which are products of synsedimentary processes [34]. In the late Rhuddanian period, the exposed area of the Kangdian Old Land on the western side of the basin continued to expand, while the embryonic form of the Xuefeng Submarine Uplift appeared on the eastern side. During the Aeronian period, the Leshan-Longnvsi Submarine Uplift on the western side of the basin was further uplifted. Due to intense compression, the Yangtze Platform formed a sedimentary pattern known as "three uplifts encircling one depression" [35]. The subsidence center of the Sichuan Basin migrated toward the central and northern regions of Sichuan. Sea levels experienced a significant drop, transforming the environment from a confined deep-water shelf into a partially confined, semi-deep to shallow-water shelf depositional environment [36].

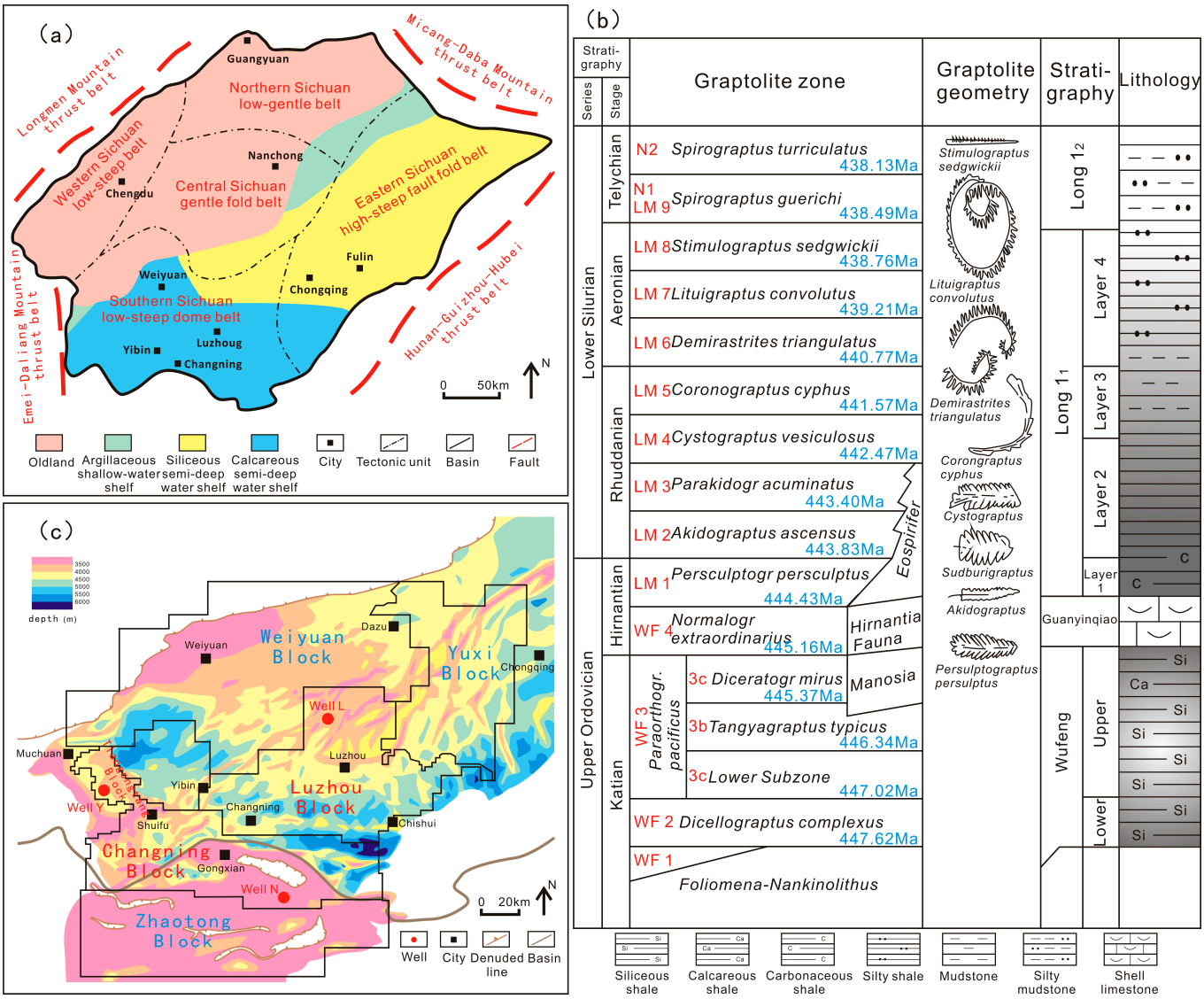

Figure 1. Geologic setting and generalized geologic column of the Sichuan Basin. (**a**) Sedimentary facies and tectonic units, modified from Lin et al. [24]; (**b**) graptolite zone and lithology in the Southern Sichuan Basin, modified from Chen et al. [37] and Ma et al. [8]; and (**c**) geographical location of the study area and burial depth, modified from Zhu et al. [6].

The Wufeng–Longmaxi shale deposited in a deep-water shelf environment is the main target for marine shale gas exploration and development in the Sichuan Basin. The Wufeng shale is predominantly composed of black shale and bioclastic limestone [38]. The Longmaxi Formation can be divided into the Long1 and Long2 members, and the Long1 member can be subdivided into two submembers from top to bottom. The second submember consists of black to dark gray limestone. The first submember is primarily composed of black shale that is rich in fossilized graptolites, exhibiting well-developed bedding. Previous researchers have identified multiple graptolite zones, including WF1-WF4 of the Wufeng Formation and LM1-LM9 of the Longmaxi Formation, in the southern Sichuan area through systematic outcrop sequence stratigraphy and graptolite fossil stratigraphic research (Figure 1b) [37,39]. Currently, this classification scheme is recognized as the scale used for division in biostratigraphic research on marine shale gas reservoirs in the southern region, specifically the Longmaxi Formation. Based on this scheme, the first submember has been subdivided into four single-layers. They are Layer 1, Layer 2, Layer 3 and Layer 4 from bottom to top [8]. Layer 1 to Layer 3 correspond to the graptolite zones LM1-LM5 in

the Rhuddanian Stage, while Layer 4 roughly corresponds to the graptolite zones LM6-LM8 in the Aeronian Stage. In this study, we further subdivided Layer 4 into Layer 4~Layer 7 according to their sedimentary environment and laminae characteristics.

Tectonically, the basin can be subdivided into five tectonic units: the Central Sichuan gentle fold belt, the Western Sichuan low-steep belt, the Northern Sichuan low-gentle belt, the Eastern Sichuan high-steep fault fold belt, and the Southern Sichuan low-steep dome belt [6]. The study areas are located in the Southern Sichuan low-sleep dome belt (Figure 1c). The Wufeng–Longmaxi shale is mainly distributed between 2000 and 4500 m. The Luzhou area is located between the Qiyue Mountain Fault Zone and the Huaying Mountain Fault Zone (Figure 2a). The fold structures within the area gradually bifurcate and spread in a broom-shaped pattern from north to south. The main fault structures are oriented in the NE, NNE, and nearly E–W directions [40]. Compared to the Changning area and Tiangongtang area (Figure 2b), the target formation in this region developed in deeper water bodies in the sedimentary period, with burial depths from 3500 to 4500 m. Previous researchers discovered a complete graptolite zone in the L10 well, indicating that the sedimentary development in the area remains continuous and stable, and almost unaffected by large-scale tectonic movements, which is beneficial for the study of sedimentary environment evolution [4]. The Tiangongtang area is located in the Yibin area in western Changning and is currently one of the least studied areas in the Sichuan Basin. The Tiangongtang structure is located within the low-fold tectonic belt and is controlled by both the eastern Sichuan fold-thrust belt and the Loushan fold belt. The structure is an irregular box-shaped anticline, with the main axis in the NW direction, showing the characteristics of the steep northeast wing and gentle southwest wing (Figure 2c). The main burial depths of the Wufeng–Longmaxi shale are between 3000 and 4000 m [41]. The Changning area is located in the northwest margin of the Upper Yangtze Plate (Figure 2d). The surface structure is controlled by folds, such as the Changning Anticline, Jianwu Syncline, and Luochang Syncline, with localized development of fractures [1]. The main body of the Changning Anticline extends in a NW–SE direction and has an overall westward inclination. It exhibits characteristics of being wider in the east and narrower in the west, with a gentle southern slope and a steep northern slope. The Wufeng–Longmaxi shale is buried at depths ranging from 2000 to 4000 m. Although there are significant variations in burial depths across different areas, the target formation exhibits similar geological characteristics [42].

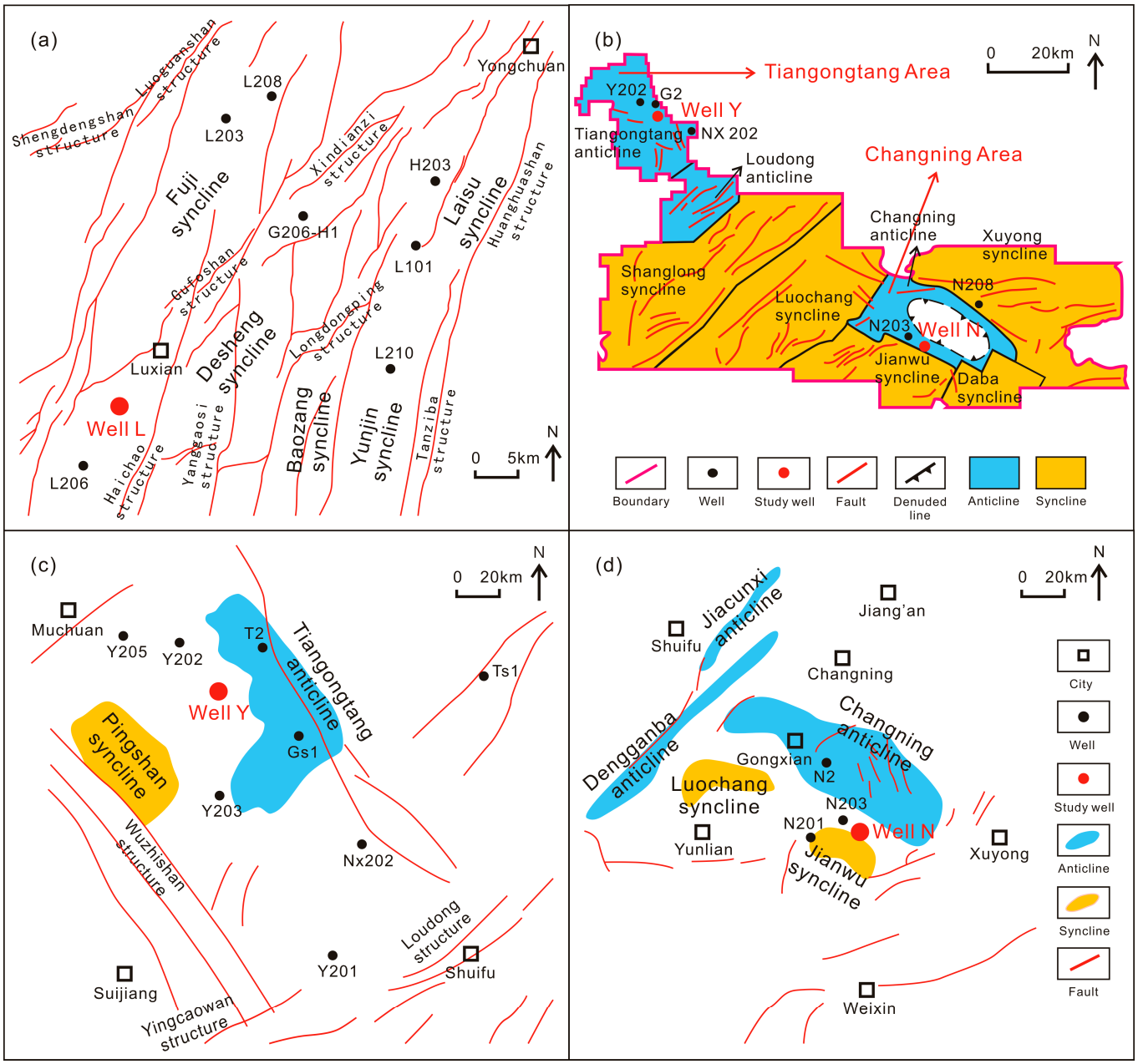

Figure 2. Geographical location of the study areas and their main structures. (**a**) Northern Luzhou area, modified from Luo et al. [40]; (**b**) Changning tectonic area; (**c**) Tiangongtang area, modified from Zhang et al. [41]; and (**d**) Changning area, modified from He et al. [42].

3. Materials and Methods

The main part of the research area is located far away from major fault zones, has not been disrupted by faults, and exhibits minimal deformation [43]. In this study, a systematic observation of the core was conducted, and samples were collected covering Wufeng–Longmaxi Formations, effectively representing the stratigraphic interval. A total of 64 shale samples were used for elemental analysis, organic petrologic analysis, and mineral composition analysis. Among these samples, 30 were selected for pore structure analysis, and 26 of them were made into thin sections for microscopic observation.

3.1. Elemental Analysis

Major element testing was performed using a Thermo iCAP 7000 series ICP–OES (Thermo Fisher Scientific, Waltham, MA, USA), following GB/T 14506.31-2019. The wavelength range was from 166 nm to 847 nm, with a spectral width of 200 nm. The radio frequency signal source operated at 27.12 MHz. The experiment procedure is described in detail by Chen et al. [29]. The quantity of the analyte component in the sample is calculated by measuring the signal intensity of the characteristic spectral line. Trace element testing was conducted using an Agilent 7700e ICP–MS (Agilent Technologies, Palo Alto, CA, USA), according to GB/T 14506.30-2010. The mass spectrometry range of the instrument was from 2 atomic mass units (amu) to 260 amu. After preparing the solution, the isotopic content of the sample was determined using the external standard ICP–MS method.

3.2. Microscopic Observations

The shale samples were dissected along the direction of vertical laminae, making sections measuring 4 cm × 4 cm. Lamina identification at the microscale was conducted using a DSX1000 digital microscope (Olympus, Beijing, China) under plane polarized light and perpendicular polarized light. Parameters such as the particle size, lamina thickness, and lamina density were analyzed by using Image-Pro Plus Version 6.0 software. The pore type and morphological observations were conducted using a TESCAN CLARA FE-SEM (Tescan, Brno, Czech Republic). Before observation, the sample was made into a rock thin section measuring 1 cm × 1 cm × 0.5 cm. Its surface was polished using a focused ion beam and sprayed with a layer of gold to enhance conductivity.

3.3. Organic Petrologic Analysis

The total organic carbon (TOC) content testing was conducted using a Leco-CS 844 Carbon-Sulfur Analyzer (LECO, San Joseph, MI, USA), according to GB/T 19145-2003. Placed approximately 0.1 g of powdered sample into a permeable crucible, removed inorganic carbon with 5% hydrochloric acid solution, and then rinsed with deionized water until the solution was neutral. Before the test, the instrument was calibrated using a standard substance (Leco 502-899: TOC = 3.19% ± 0.03%). The sample was mixed with iron filings and tungsten–tin combustion enhancers and burned in a drying oven at 1100 °C to obtain the TOC content.

The vitrinite reflectance (R_o) test was conducted using a MSP 400 Microfluorescence Spectrometer (J&M, Essingen, Rhineland-Palatinate, Germany), according to SY/T 5124-2012. Oil was dropped onto the sample surface, and the appropriate vitrinite measurement area was selected using a rotating sample stage. At least 20 sets of randomly selected reflectance values were measured, and the maximum, minimum, and average values, as well as the standard deviation of the reflectance coefficient were recorded.

Carbon and oxygen isotope analysis was conducted using a MAT 253 Stable Isotope Mass Spectrometer (Thermo Fisher Scientific, Waltham, MA, USA), according to SY/T 5238-2019. Based on the collected carbon isotope composition of CO_2, the following equation can be used to calculate the δ value: $\delta = [(R_{sample}/R_{standard}) - 1] \times 1000$, where R can be either $^{18}O/^{16}O$ or $^{13}C/^{12}C$. To determine the type of kerogen, we compare the relative Pee Dee Belemnite (PDB) value with the known δ values of different kerogen types. Different types of kerogens have specific ranges of carbon isotope compositions, allowing us to determine the kerogen type of the sample through comparison.

3.4. Mineral Composition Analysis

The mineral composition experiment was carried out using a Smart Lab SE X-ray Diffractometer (Rigaku, Tokyo, Japan), according to SY/T 5163-2018. The maximum power of the X-ray generator was 3 kW. The scanning speed was 20° (2θ)/min. For whole-rock minerals, the scanning range was from 3° to 45°, while for clay minerals, the scanning range was from 2.5° to 30°. The data analysis software that was used was Rockquan and Clayquan II, which allows for the quantitative calculation of the mineral composition.

3.5. Pore Structure Analysis

The high-pressure mercury injection experiment was conducted using an AutoPore IV 9500 Porosity Analyzer (Micromeritics, Shanghai, China), according to GB/T 29171-2012. The instrument had a maximum operating pressure of 60,000 psi (228 MPa), and the pore size measurement range was from 5 nm to 1000 μm (3 nm to 300 μm). The correlation between the pore size and applied pressure can be described by the Washburn equation, which can be used to calculate the pore volume and specific surface area.

The N_2 and CO_2 adsorption experiment was performed using an ASAP 2460 Surface Area and Pore Size Analyzer (Micromeritics, Norcross, GA, USA), according to SY/T 6154-1995 and GB/T 21650.3-2011, respectively. The N_2 adsorption experiment required approximately 1 g of powder with a particle size of approximately 200 mesh. After drying, the sample needed to be degassed under vacuum for 24 h. Then, samples were placed in the adsorption station and subjected to adsorption–desorption experiments within the relative pressure range of 0.001 to 0.995. The experiment was conducted at a temperature of 77.35 K (−195.8 °C), which was achieved using liquid nitrogen. The pressure range for the experiment was from 0.1 KPa to 133 KPa. The pore size measurement range was from 0.926 nm to 500 nm, with an accuracy of ±0.02 nm. The obtained data were processed using the Brunauer–Emmett–Teller (BET) model and the Barrett–Joyner–Halenda (BJH) model. For CO_2 adsorption experiments, the relative pressure range was from 0.001 to 0.018. The pore size measurement range was from 0.402 nm to 0.926 nm, with an accuracy of ±0.02 nm. The pore volume, specific surface area, and pore size distribution were processed using the Dubinin–Astakhov (D-A), Dubinin–Radushkeyich (D-R), and density functional theory (DFT) models.

4. Results

4.1. Shale Lithological and Mineralogical Characteristics

The Wufeng–Longmaxi shale formations in the study area are characterized by large thickness, high TOC content, well-developed laminations and complex pore systems, making it an ideal object for studying the development characteristics of deep shale. Figure 3 indicates that the lithology of the Wufeng Formation is mainly composed of silty mudstone and black siliceous shale. The sedimentation in the Tiangongtang area is influenced by bioturbation and does not develop laminae. Numerous clustered pyrite can be observed on the surface of shale samples. The bottom of the Longmaxi Formation is composed of black carbonaceous shale, with abundant fossils and well-developed laminations. The middle section of the Longmaxi Formation consists of dark graptolite-rich shale, interbedded with gray silty shale. The top section is characterized by gray-black silty mudstone and shale.

The mineral composition is closely related to the sedimentary environment, diagenesis, and burial depth. Table 1 and Figure 4a show that shales in the study area are predominantly composed of clay minerals and quartz, with average contents of 33.7% and 32.6%, respectively. The main composition of clay mineral is illite, with an average content of 68.6%, followed by a mixed layer of illite and smectite (I/S) and chlorite. Kaolinite has been extensively transformed into illite and I/S. The average content of siliceous minerals is 39.4%, including biogenic quartz and siliceous organisms. The average content of carbonate minerals is 26.9%, mainly derived from biological and chemical precipitation during sedimentation. Based on the mineral composition, shale can be classified into four major categories (siliceous shale, argillaceous shale, calcareous shale, and mixed shale) and sixteen subcategories (Figure 4b). The dominant lithofacies in the target layer are argillaceous/siliceous mixed shale lithofacies and argillaceous-rich siliceous shale lithofacies.

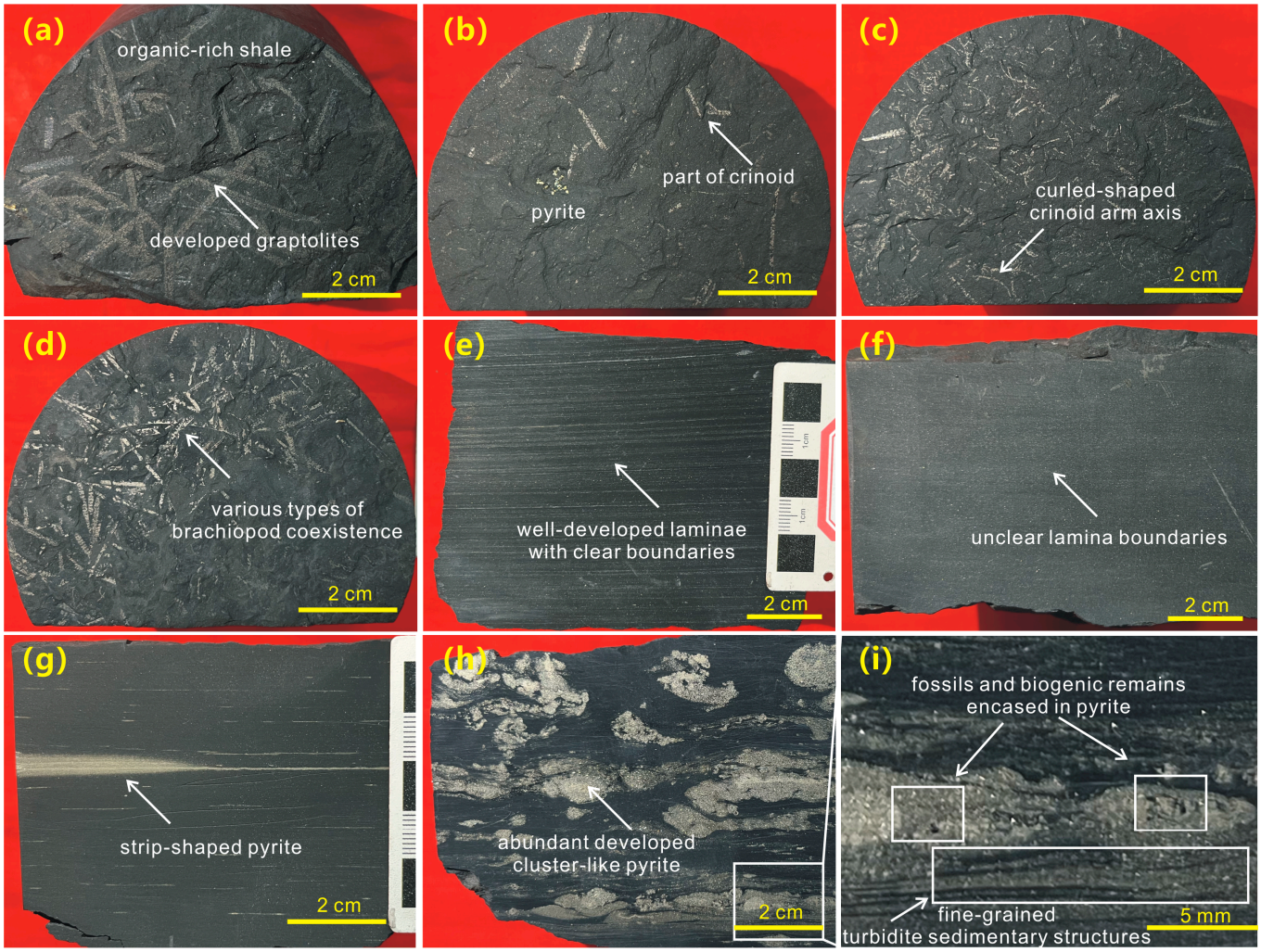

Figure 3. Lithological characteristics of the typical samples in the study area. (**a**) N4, Layer 3, LM4-5, black argillaceous-rich siliceous shale; (**b**) Y9, Layer 4, LM5-6, black argillaceous/siliceous mixed shale; (**c**) Y8, Layer 5, LM6, gray black argillaceous/siliceous mixed shale; (**d**) L4, Layer 6, LM7, black siliceous-rich argillaceous shale; (**e**) Y1, Layer 7, well-developed laminae, mixed shale; (**f**) L2, Layer 6, indistinct laminae, argillaceous/carbonate mixed shale; (**g**) L11, Layer 1, well-developed laminae, striped pyrite, mixed shale; (**h**) Y12, Wufeng, undeveloped laminae, abundant clustered pyrite, argillaceous-rich calcareous shale; and (**i**) is an enlarged image of (**h**), showing the developmental characteristics of bioturbation and cluster-type pyrite.

Table 1. Mineralogy composition of the Wufeng–Longmaxi Shale samples in study area.

Sample	Stratum	Depth (m)	Quartz	Feldspar	Calcite	Dolomite	Pyrite	Clay	Kaolinite	Illite	Chlorite	I/S *
L1	Layer 7 *	4053.42	28.8	10	2.9	13.1	6	39.2	2	84	13	1
L2	Layer 6	4058.05	17.4	4.5	18.2	19.7	4	36.2	4	64	9	23
L3	Layer 6	4064.29	11.9	2.6	63.6	8.2	1.1	12.6	0	64	0	36
L4	Layer 6	4072.31	27	7.1	8.5	13.7	2.7	41	0	85	14	1
L5	Layer 5	4078.24	35.1	7.2	7.3	10.6	3.4	36.4	0	89	7	4
L6	Layer 5	4085.03	29.9	15.9	7.8	11.1	2.9	32.4	0	87	12	1

Table 1. *Cont.*

Sample	Stratum	Depth (m)	Quartz	Feldspar	Calcite	Dolomite	Pyrite	Clay	Kaolinite	Illite	Chlorite	I/S *
L7	Layer 4	4095.14	26.4	13	7.1	6.1	7.4	40	0	87	10	3
L8	Layer 3	4103.53	47.2	4.8	2	1.7	3.4	40.9	0	68	0	32
L9	Layer 2	4107.64	56.9	1.9	3.6	6.3	3.8	27.5	0	52	6	42
L10	Layer 2	4111.08	49.9	4	6.6	13.3	6.7	19.5	1	90	7	2
L11	Layer 1	4114.07	36.1	4.7	17.4	4.8	3.4	33.6	0	45	0	55
L12	Wufeng	4119.40	33.3	2.1	2	0.7	14	47.9	3	22	2	73
Y1	Layer 7	3846.34	29	8.3	8.6	12.2	2.2	39.7	3	75	21	1
Y2	Layer 6	3851.28	34	8.8	11.5	14.8	2.5	28.4	7	33	18	42
Y3	Layer 6	3852.53	27.4	10.9	23	17.1	2.3	19.3	0	74	20	6
Y4	Layer 6	3856.39	24.6	7.7	15.6	10.2	3.1	38.8	1	79	14	6
Y5	Layer 6	3860.28	26.7	5.9	13.4	6.5	3.2	44.3	0	67	18	15
Y6	Layer 6	3861.09	2.5	4.2	1	1.7	22.3	68.3	0	31	5	64
Y7	Layer 5	3862.89	27.3	5.4	12.5	11.3	4.3	39.2	0	44	15	41
Y8	Layer 5	3868.25	42.4	5.5	2.8	0	3.5	45.8	0	49	13	38
Y9	Layer 4	3875.43	32.7	8.6	10.3	9.9	3.4	35.1	8	55	22	15
Y10	Layer 3	3879.06	45.7	9.6	3.5	4.4	3	33.8	2	73	16	9
Y11	Layer 2	3882.35	30	3.6	5.5	12.8	34.3	13.8	2	81	16	1
Y12	Wufeng	3887.91	8.3	1.6	15.8	34.5	13.1	26.7	1	79	17	3
N1	Layer 5	2533.39	33.8	19.4	13.5	6	1.4	25.9	3	78	17	2
N2	Layer 5	2542.65	32.1	7.1	7.1	1.8	2.8	49.1	1	71	27	1
N3	Layer 4	2559.23	50.9	4.7	9.4	3.5	3.1	28.4	1	74	19	6
N4	Layer 3	2560.67	34	7.2	14	18	4	22.8	1	87	8	4
N5	Layer 3	2565.34	44.3	3.7	14.4	17	2.7	17.9	3	86	8	3
N6	Layer 2	2574.85	52	5	9.9	2.6	3.3	27.2	2	85	10	3

* Layer 7 is the seventh single layer of the first submember of Long1. I/S is the mixed layer of illite and smectite.

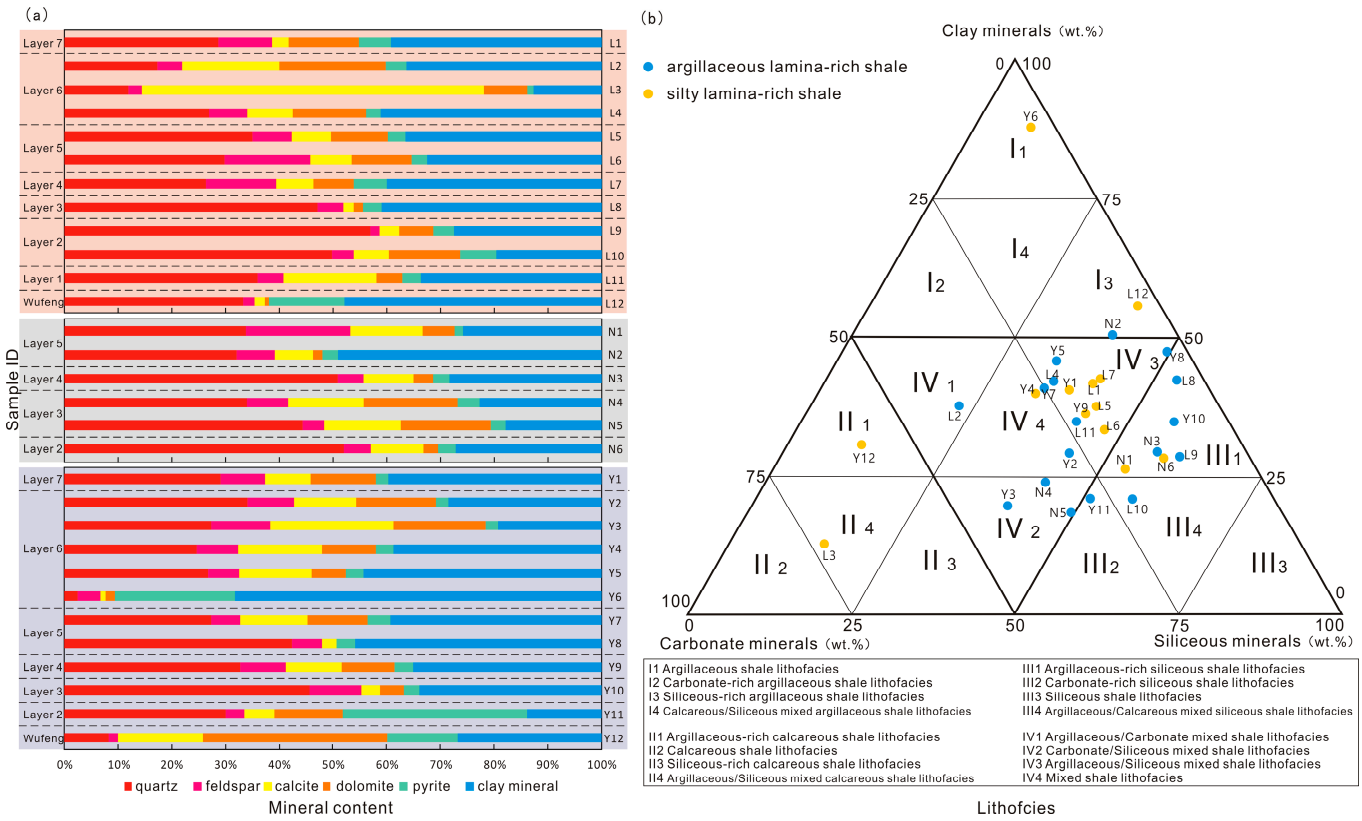

Figure 4. (**a**) Mineral composition; (**b**) lithofacies type of shales from the Wufeng–Longmaxi in the study area.

4.2. Shale Sedimentary Environment

4.2.1. Paleoclimate

The paleoclimate can be studied using climate-sensitive elements and the chemical index of alteration (CIA) [44]. Under dry climate conditions, atmospheric precipitation decreases, and surface water evaporates extensively, resulting in the abundant precipitation and deposition of elements such as Ca, Mg, K, Na, Sr, and Ba in the basin. Researchers have utilized the Sr/Cu ratio for paleoclimate research. When Sr/Cu > 10, it indicates an arid climate, while Sr/Cu < 10 represents a humid climate [45]. The CIA = $[Al_2O_3/(Al_2O_3 + Na_2O + CaO^* + K_2O)] \times 100$, which can also reflect the extent of chemical weathering. A CIA < 50 represents a low degree of weathering and a cold–arid climate. A 50 < CIA < 65 indicates a moderate degree of weathering and a semiarid climate. A 65< CIA < 80 represents a moderate degree of weathering and a semihumid climate. A CIA > 80 signifies a high degree of weathering and a humid climate. The results in Table 2 and Figure 5a indicate that the CIA values of the Wufeng–Longmaxi shale range from 63 to 79, with an average of 72.5. The intersection diagram of the CIA and Sr/Cu test results suggests that the study area during the depositional period was generally characterized by a moderately weathered semihumid climate.

Table 2. Major and trace elements analysis of the Wufeng–Longmaxi Shale samples in the study area.

Sample	Depth (m)	Mo_{EF}	U_{EF}	CIA	Sr/Cu	U/Th	Sr/Ba	Mn/Fe	U (ppm)	P (%)	P/Ti	Al (%)	Ti (%)	Zr (%)
L1	4053.42	13.90	3.16	72.38	5.76	0.84	0.21	0.007	15.85	0.11	0.17	14.41	0.60	152.84
L2	4058.05	5.68	0.80	69.33	15.23	0.26	0.13	0.027	2.60	0.15	0.30	9.35	0.49	164.29
L3	4064.29	19.19	2.77	67.73	15.63	0.62	0.28	0.020	3.41	0.08	0.50	3.53	0.16	55.91
L4	4072.31	7.42	1.82	76.22	5.76	0.70	0.25	0.07	10.37	0.10	0.20	16.31	0.50	95.29
L5	4078.24	6.25	1.40	76.14	4.68	0.70	0.23	0.004	7.18	0.12	0.23	14.73	0.51	52.02
L6	4085.03	7.84	1.75	75.09	4.61	0.73	0.25	0.04	7.51	0.11	0.27	12.31	0.41	30.90
L7	4095.14	7.87	2.27	72.67	35.47	0.65	0.30	0.08	10.13	0.10	0.19	12.79	0.50	102.30
L8	4103.53	20.40	2.99	70.28	1.75	1.09	0.04	0.006	13.70	0.12	0.18	13.14	0.65	93.20
L9	4107.64	36.85	3.98	71.27	1.57	1.75	0.05	0.005	13.06	0.12	0.27	9.41	0.43	60.65
L10	4111.08	45.20	10.41	72.11	4.80	2.33	0.35	0.009	24.00	0.10	0.34	6.62	0.29	56.20
L11	4114.07	55.48	10.19	70.07	3.74	4.57	0.11	0.013	38.56	0.10	0.17	10.87	0.56	101.92
L12	4119.40	10.86	1.46	73.30	1.94	0.56	0.04	0.004	6.90	0.05	0.09	13.58	0.59	184.26
Y1	3846.34	4.36	2.20	75.06	12.33	0.65	0.26	0.012	11.63	0.10	0.19	15.15	0.52	89.90
Y2	3851.28	6.99	3.64	71.53	9.88	0.82	0.17	0.017	17.23	0.12	0.20	13.60	0.61	189.90
Y3	3852.53	4.60	1.87	69.02	31.06	0.38	0.50	0.033	5.58	0.16	0.37	8.59	0.43	185.90
Y4	3856.39	7.93	3.08	73.58	13.94	0.89	0.27	0.018	13.93	0.13	0.30	12.98	0.45	103.90
Y5	3860.28	8.33	4.76	74.60	6.15	1.72	0.19	0.013	20.60	0.12	0.28	12.43	0.44	96.10
Y6	3861.09	8.37	1.88	79.09	7.74	0.36	0.09	0.004	13.58	0.11	0.10	20.75	1.09	907.69
Y7	3862.89	7.62	3.08	73.63	50.09	0.79	0.20	0.011	13.46	0.10	0.22	12.53	0.44	87.06
Y8	3868.25	6.38	1.83	74.07	2.78	0.83	0.13	0.005	9.26	0.09	0.17	14.50	0.51	69.90
Y9	3875.43	10.40	2.76	70.20	5.68	0.92	0.21	0.017	12.19	0.10	0.19	12.69	0.54	133.46
Y10	3879.06	33.94	6.70	71.54	2.93	1.98	0.15	0.008	17.86	0.08	0.29	7.65	0.29	47.75
Y11	3882.35	47.01	9.06	72.54	20.13	2.46	0.36	0.09	22.70	0.12	0.43	7.19	0.28	52.80
Y12	3887.91	7.28	1.97	73.89	9.86	0.31	0.51	0.012	5.80	0.01	0.04	8.47	0.42	140.10
N1	2533.39	3.21	1.35	72.68	7.27	0.38	0.94	0.006	7.12	0.09	0.15	15.20	0.62	163.78
N2	2542.65	3.97	1.28	74.91	5.13	0.42	0.60	0.005	7.39	0.09	0.15	16.53	0.62	75.10
N3	2559.23	14.63	3.35	74.69	4.06	1.03	0.75	0.006	12.83	0.10	0.25	10.99	0.40	56.18
N4	2560.67	18.30	4.00	73.31	4.86	1.06	0.80	0.005	12.32	0.09	0.26	8.85	0.35	61.67
N5	2565.34	29.87	7.29	70.17	7.20	1.50	1.41	0.012	21.10	0.08	0.21	8.31	0.39	83.80
N6	2574.85	50.79	12.67	69.14	14.39	2.31	2.09	0.036	22.50	0.05	0.19	5.10	0.25	71.30

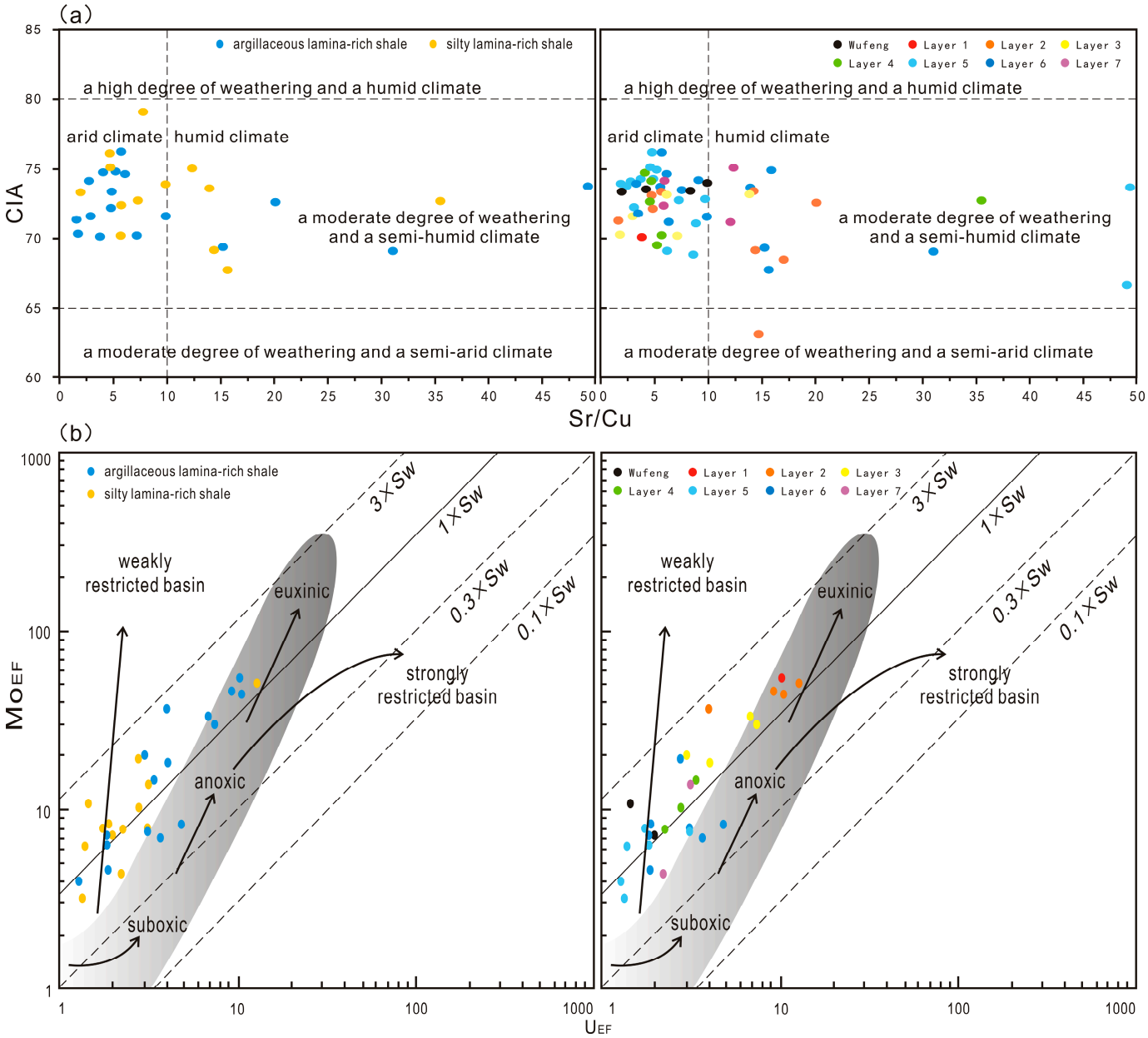

Figure 5. Paleoclimate and paleoredox characteristics of the study area. (**a**) Crossplots of CIA-Sr/Cu of Wufeng–Longmaxi; (**b**) crossplots of Mo_{EF}-U_{EF} of Wufeng–Longmaxi, modified from Tribovillard et al. [46]. Sw represents the ratio of Mo_{EF} and U_{EF} in seawater, Sw = 7.9. The diagonal lines represent multiples (0.1, 0.3, 3) of the Sw. The gray field represents the unrestricted marine trend.

4.2.2. Paleoredox Conditions

The indicators for discriminating redox conditions in sedimentary water bodies include sedimentological features, such as pyrite and biological fossils, trace element geochemical indicators, and certain biomarker compounds [47]. Due to the high degree of shale evolution in Wufeng–Longmaxi, the biomarker test results may not accurately reflect the information in the sedimentary period. Previous studies have shown that V, Cr, Ni, U, Th, Mo, etc. are redox sensitive elements in fine-grained sediments, and DOP, U/Th, U/Mo, Ni/Co, V/Cr, V/(V + Ni), Ua, etc. are reliable indicators for determining redox conditions [48–50]. The enrichment coefficient (X_{EF}) can reflect the enrichment or depletion of a certain trance element and is commonly used in discriminating the redox environments. The calculation formula for the enrichment factor of X element is X_{EF} =

(X/Al)sample/(X/Al)ucc. The (X/Al)sample represents the ratio of the X content to Al content in the sample, while the (X/Al)ucc comes from the standardized values of the upper continental crust. The ratios of (Mo/Al)ucc and (U/Al)ucc are 0.19 and 0.35, respectively. A $X_{EF} > 1$ indicates enrichment of the X element. A $X_{EF} < 1$ indicates depletion of the X element [48]. The study primarily relies on Mo_{EF}-U_{EF} synergistic curves supplemented by U/Th results to characterize the redox conditions during the sedimentary period. The results in Table 2 and Figure 5b indicate that the Mo_{EF} values range from 2.25 to 118.68, with an average of 29.83, while the U_{EF} values range from 0.60 to 40.47, with an average of 6.88. The enrichment level of Mo is significantly higher than that of U. The Mo_{EF}/U_{EF} ratio ranges from 0.3 × SW to 3 × SW, the Wufeng and Layer4~Layer 7 indicate a weakly restricted environment, while Layer1~Layer3 indicate a relatively strong restricted environment. A U/Th >1.25 indicates an anoxic environment. A 0.75 < U/Th < 1.25 suggests a suboxic environment. A U/Th < 0.75 presents an oxic environment. The average U/Th ratio of the samples from Wufeng and Layer 4~Layer 7 is 0.64, indicating an oxic environment. The average U/Th ratio of the samples from Layer 1~Layer 3 is 2.29, indicating an anoxic environment.

4.2.3. Paleowater Depth, Paleosalinity, and Paleoproductivity

The accumulation and dispersion of elements in sediments are closely related to the paleo-water depth during the sedimentary period. Researchers often use the Mn/Fe ratio and U content to determine water depth and water dynamic conditions during sedimentary periods. Both of them are positively correlated with paleo-water depth. The results in Table 2 indicate that the Mn/Fe ratios in the studied shale area range from 0.002 to 0.058, while the U contents vary significantly between 1.7 and 61.1 ppm. Layer 1~Layer 3 show the greatest depth with weaker energy conditions in water during deposition. The water depth was relatively shallow during deposition of the Wufeng Formation and Layer 4~Layer 7, with stronger energy conditions of the water. It is worth noting that elemental and ratio analyses can only indicate relative changes in water depth. To reconstruct the specific changes in paleo-water depth in the sedimentary basin, a comprehensive analysis concerning geological background, sedimentary evolution, and changes in basin area, lithofaices and biofacies is needed [51].

The Sr/Ba is an important method to reconstruct the paleosalinity. A Sr/Ba < 0.2 indicates a freshwater environment. A 0.2 < Sr/Ba < 0.5 indicates a brackish water environment. A Sr/Ba > 0.5 indicates a saltwater environment [52]. The results in Table 2 indicate that the Sr/Ba values in the Wufeng–Longmaxi shales range from 0.04 to 1.54. Salinity changes in water bodies are influenced by a variety of factors, including precipitation, sea level changes, and biological activity. During the ice age (Upper Wufeng Formation), the climate cooled, leading to the extinction of warm-water organisms, a decrease in rainfall, and a drop in sea levels, resulting in an increase in salinity. After the ice age (Layer 1), the climate warmed, causing glaciers to melt and sea levels to rise. This led to a flourishing of planktonic organisms and a decrease in salinity.

Paleoproductivity plays an important role in organic matter enrichment and hydrocarbon generation potential. The contents and distribution characteristics of P in sediments are closely related to the primary productivity of source rocks and the supply of organic matter. The P/Ti can eliminate the influence of terrestrial detritus and better characterize the nutrient status of water bodies [53]. The P/Ti ratios range from 0.035 to 0.503, with an average of 0.206, which is higher than the average of 0.15 for marine shale, indicating high productivity during the whole sedimentary period.

4.3. Lamination Characterization

4.3.1. Composition, Texture and Structure of Lamina

Based on the composition, shale laminations can be divided into siliceous laminae, clay laminae, calcareous laminae, and organic laminae. All four types of laminae are developed in the Wufeng–Longmaxi shale, and their scale of development is closely related to the corresponding mineral content. Siliceous laminae have a lighter color, appearing white or grayish white in plane polarized light and pale yellow in perpendicular polarized light. They are primarily composed of quartz, sodium feldspar, and small amounts of calcite (Figure 6a,b). The siliceous laminae primarily exhibit a continuous parallel plate-like distribution, with boundaries distinct from those of the other laminae. Local occurrences of parallel microfractures can be observed (Figure 6b,e). The clay laminae have a relatively dark color, appearing dark gray in plane polarized light and brown in perpendicular polarized light (Figure 6e,f). The main components of the laminae are clay minerals, primarily consisting of chlorite and illite. The clay laminae are primarily characterized by a parallel plate-like distribution, with a small amount exhibiting a continuous or discontinuous parallel wavy pattern. The interfaces between the laminae are relatively indistinct, and there are no developed internal fractures. The clay laminae are often closely interbedded with other laminae. The calcareous laminae have a color that ranges between that of the siliceous and clay laminae, i.e., light gray or gray in plane polarized light and yellow in perpendicular polarized light. The main components of the calcareous laminae are calcite and dolomite. The calcareous laminae are mostly characterized by a continuous parallel plate-like distribution, with poor clarity at the interfaces between the laminae. Previous studies have shown that when magnified to the nanometer scale, local transverse fractures and biogenic debris such as graptolites and radiolaria can be observed (Figure 6h). The organic laminae appear black under both plane-polarized light and perpendicular polarized light. They exhibit a continuous parallel plate-like distribution with distinct boundaries. Sometimes, they are found in association with siliceous and clay minerals (Figure 6b–d). The Wufeng Formation is influenced by disturbance, resulting in a blocky profile. It contains abundant pyrite and biogenic debris, such as radiolaria, in some areas (Figure 6g–i).

According to particle size, we classify the laminae that are primarily composed of particles with diameters <31.2 μm as argillaceous laminae (with an argillaceous particle content >50%) [26]. Similarly, the laminae that are mainly composed of particles with diameters ranging from 31.2 μm to 62.5 μm are classified as silty laminae (with a silty particle content >50%). Argillaceous laminae have a darker color and are often referred to as dark laminae, while silty laminae have a lighter color and are commonly referred to as light laminae (Figure 6). Microscopic observations and statistical analysis reveal that the lower part of the Wufeng Formation in the study area exhibits a massive shale texture with poorly developed laminae. Toward the top, there are thin silty laminae, with an average silty particle content of 67.5%. Layer 1~Layer 3 are primarily characterized by the development of argillaceous laminae, with an average argillaceous particle content of 62.5%. In areas with greater burial depths, Layer 4 is primarily characterized by the development of silty laminae, with a silty particle content of 51.7%. In areas with shallower burial depths, Layer 4 is mainly composed of argillaceous laminae, with an argillaceous particle content of 62.9%. The characteristics of Layer 5~Layer 7 development are the most complex, with frequent alternations between argillaceous laminae and silty laminae. However, from bottom to top, the degree of silty laminae development gradually increases.

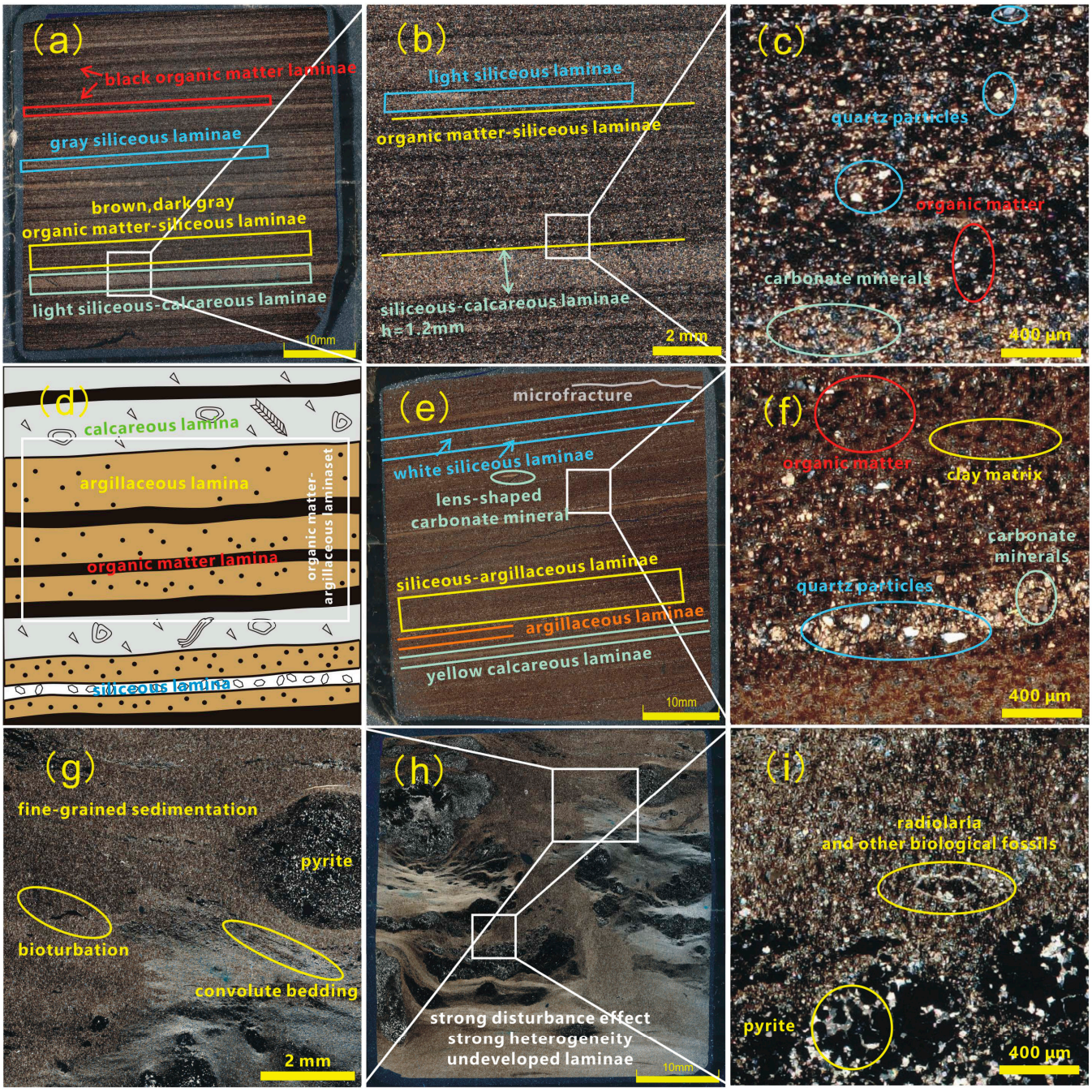

Figure 6. Characteristics of laminae development in the study area. (**a**) N6, Layer 3, 4 cm × 4 cm slice, perpendicular polarized light, argillaceous-rich siliceous shale, and the laminae are highly developed and exhibit a continuous parallel plate-like distribution; (**b**) is an enlarged image of (**a**), showing a 1.2 mm-wide calcareous lamina, and organic matter coexists with siliceous minerals, forming an organic matter-siliceous laminaset; (**c**) is an enlarged image of (**b**), in which white quartz, black organic matter, carbonate minerals and clay matrix can be observed; (**d**) schematic diagram of the characteristics of laminae development; (**e**) Y1, Layer 7, 4 cm × 4 cm slice, perpendicular polarized light, mixed shale, and laminae are developed and exhibit a continuous parallel plate-like distribution; (**f**) is an enlarged image of (**e**), in which organic matters coexist with clay minerals, and quartz and calcite are observed; (**g**) is an enlarged image of (**h**), demonstrating the impact of bioturbation on the development of lamination; (**h**) Y12, Wufeng, 4 cm × 4 cm slice, perpendicular polarized light, homogeneous argillaceous-rich calcareous shale, with developed pyrite; and (**i**) is also an enlarged image of (**g**), with developing pyrite and clay matrix, and biofossils and debris, such as radiolarians, can be observed.

4.3.2. Composition, Texture and Structure of the Laminaset

A laminaset is formed by the integration of two or more laminae with similar mineral compositions, structures, and geometric relationships. The thicknesses generally range from a few millimeters to several centimeters [54]. If the proportion of argillaceous laminae is greater than 50%, it is classified as an argillaceous laminaset; otherwise, it is classified as a silty laminaset (Figure 7). In Wufeng–Longmaxi, the thickness of argillaceous laminaset development is generally greater than that of silty laminasets. The argillaceous laminasets in Layer 1~Layer 3 have the greatest thickness, averaging 0.28 cm, which is twice the thickness of Layer 5~Layer 7. The average thickness of silty laminasets in Layer 4~Layer 7 is 0.13 cm, which is generally higher than the thickness of Layer 1~Layer 3. Both the argillaceous laminasets and silty laminasets show good overall continuity, mostly occurring as plate-like parallel distributions (Figure 7a). In some samples, the laminasets are discontinuously distributed or exhibit a curved distribution (Figure 7b).

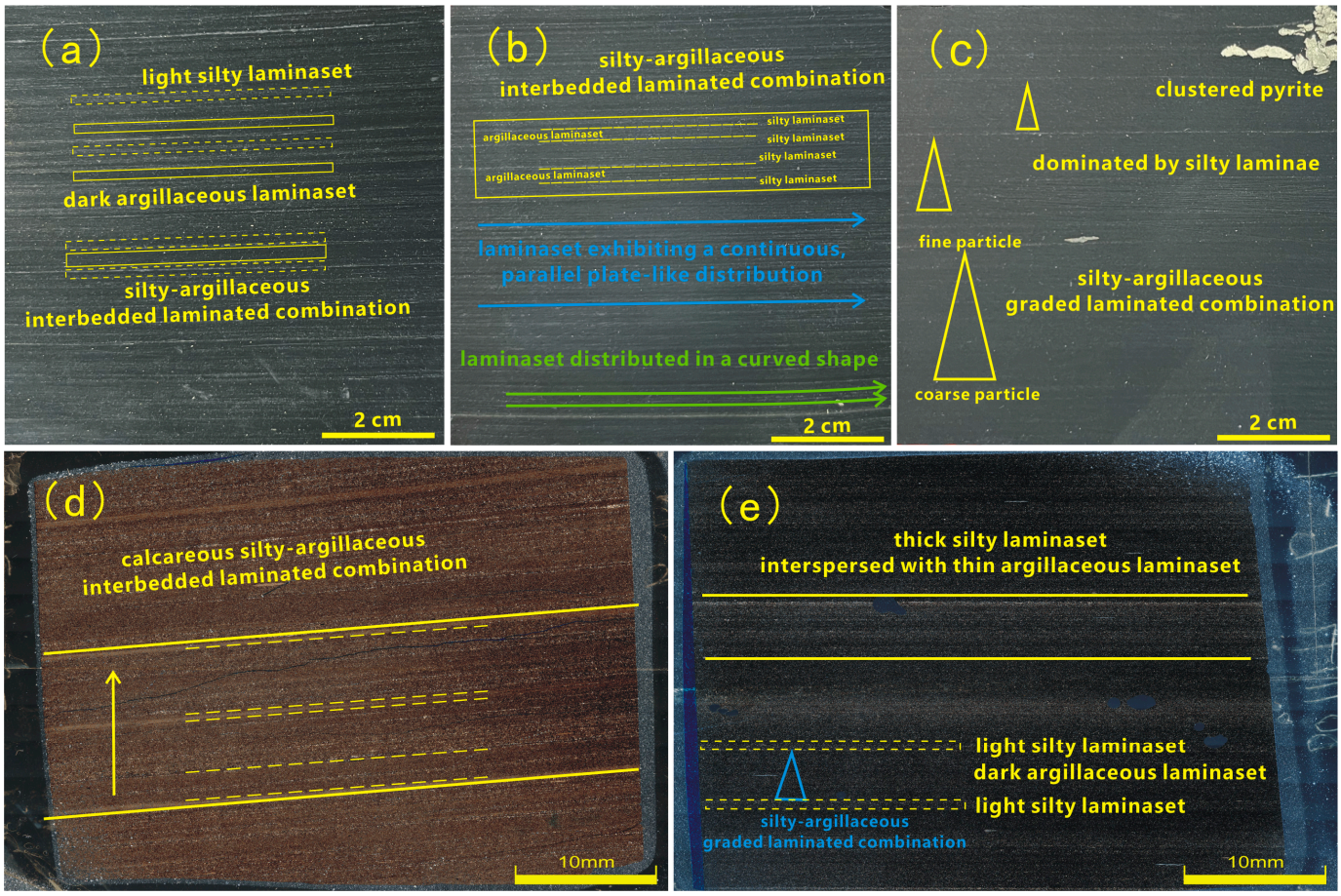

Figure 7. Characteristics of laminaset development in the study area. (**a**) L6, Layer 5, argillaceous/siliceous mixed shale, and the laminae are highly developed and exhibit a continuous parallel plate-like distribution; (**b**) Y1, Layer 7, mixed shale, with developed laminae that are the silty-argillaceous interbedded type, and local laminae exhibit a curved shape; (**c**) L8, Layer 3, argillaceous-rich siliceous shale, with a thick argillaceous laminaset and a normally graded laminaset; (**d**) Y1, Layer 7, 4 cm × 4 cm slice, perpendicular polarized light, mixed shale that is the silty-argillaceous interbedded type, with more developed silty laminae, and the boundaries between laminasets are blurry; and (**e**) L10, Layer 2, 4 cm × 4 cm slice, perpendicular polarized light, argillaceous/carbonate mixed siliceous shale that is the silty-argillaceous transitional type, with more developed argillaceous laminae, and the boundaries between laminasets are clear.

According to the stacking relationships and grain size characteristics, the laminasets are classified into three types: silty-argillaceous transitional type, silty-argillaceous interbedded type, and homogeneous type. These different types of combinations of lamina reflect changes in sedimentary conditions, including fluctuations in sedimentary energy and changes in the sediment supply. The silty-argillaceous transitional type is typically associated with turbidity currents, density flows, bottom currents, and periodic climatic variations [24]. The grain size in the normally graded laminaset decreases from bottom to top (Figure 7c,e), while the grain size in the reverse graded laminaset increases from bottom to top. They are mainly developed in Layer 2~Layer 3, exhibiting a continuous parallel plate-like distribution. Typically, the lower interfaces are clear, while the upper surfaces are relatively blurred, indicating a period of weak hydraulic processes and low input of terrestrial clastic sediments. The silty-argillaceous interbedded type consists of frequent alternations between thin argillaceous laminae and silty laminae. They often exhibit a continuous parallel plate-like distribution and have distinct differences in brightness, making their interfaces clear and distinguishable (Figure 7a,b,d). This type is primarily developed in Layer 4~Layer 7, indicating an increase in hydraulic conditions during the depositional period and an influx of terrestrial clastic sediments. The homogeneous type refers to a relatively uniform combination of lamina throughout the rock formation, without obvious layering or transitions. It occurs in the Wufeng Formation and is associated with rapid settling, suspension settling, bioturbation, and postdiagenetic processes [28].

4.4. Shale Reservoir Characterization

4.4.1. Organic Geochemical Characteristics

The results in Table 3 indicate that the TOC contents of the Wufeng–Longmaxi shale in the study area range from 0.78% to 6.46%, with an average of 3.09%. The shale exhibits a high organic abundance, suggesting a favorable source for potential hydrocarbon generation. The average TOC content of the Wufeng shale is 2.13%, which is lower than the 3.16% observed in Longmaxi. The $\delta^{13}C$ values of the samples are less than −28‰, indicating the kerogen is Type I, and the hydrocarbon source material mainly comes from algal deposits and planktons, with a significant hydrocarbon generation potential. The R_o values of the samples are distributed between 2.39% and 2.66%, with an average of 2.56%. Kerogens are in the highly mature to overmature stage, indicating a predominant production of dry gas.

Table 3. Organic geochemical test results and porosity of the Wufeng–Longmaxi Shale samples.

Sample	Depth (m)	TOC (wt.%)	R_o (%)	$\delta^{13}C$ (‰)	Type *	Porosity (%)
L1	4053.42	1.84	2.48	−30.0	I	4.65
L2	4058.05	2.39	2.39	−27.7	II_1	5.23
L3	4064.29	0.78	2.51	−29.9	I	6.67
L4	4072.31	2.33	2.49	−29.9	I	6.15
L5	4078.24	2.50	2.48	−29.8	I	6.20
L6	4085.03	2.97	2.47	−29.2	I	6.03
L7	4095.14	2.12	2.50	−29.6	I	4.51
L8	4103.53	4.69	2.45	−29.8	I	6.15
L9	4107.64	4.77	2.45	−30.4	I	6.85
L10	4111.08	5.49	2.54	−30.3	I	6.27
L11	4114.07	6.46	2.45	−30.2	I	6.38
L12	4119.4	2.22	2.39	−30.7	I	3.53
Y1	3846.34	2.11	2.61	−29.9	I	3.40

Table 3. *Cont.*

Sample	Depth (m)	TOC (wt.%)	R_o (%)	$\delta^{13}C$ (‰)	Type *	Porosity (%)
Y2	3851.28	2.89	2.64	−29.2	I	5.54
Y3	3852.53	3.14	2.63	−27.9	II_1	3.59
Y4	3856.29	0.95	2.64	−29.9	I	2.34
Y5	3860.28	3.07	2.66	−30.0	I	1.91
Y6	3861.09	0.83	2.62	−30.4	I	2.44
Y7	3862.89	2.75	2.62	−30.2	I	4.52
Y8	3868.25	2.91	2.61	−29.8	I	5.21
Y9	3875.43	2.97	2.60	−29.9	I	4.11
Y10	3879.06	5.77	2.63	−30.5	I	7.12
Y11	3882.35	5.10	2.60	−30.5	I	6.15
Y12	3887.91	2.03	2.65	−30.3	I	4.31
N1	2533.39	1.47	2.58	−28.8	I	3.79
N2	2542.62	2.20	2.59	−29.3	I	6.08
N3	2559.23	3.72	2.61	−30.2	I	6.63
N4	2560.67	3.76	2.65	−30.3	I	6.15
N5	2565.34	4.50	2.56	−30.5	I	6.80
N6	2574.85	3.86	2.64	−29.8	I	6.74

* Type-I with $\delta^{13}C$ less than −28‰, type-II_1 with $\delta^{13}C$ of −28‰-−26.5‰, type-II_2 with $\delta^{13}C$ of −26.5‰-−25‰, and type-III with $\delta^{13}C$ more than −25‰.

4.4.2. Porosity

The shale reservoir capability and shale gas occurrence primarily depend on the properties of the reservoir space, including porosity, pore type, and the characteristics of pore structure development [21]. The shale porosity values of Longmaxi in the study area range from 1.91% to 7.12%, with an average of 5.18%. The average porosities of wells L and Y are 5.72% and 4.22%, respectively, which are slightly lower than that of well N (with an average of 6.03%). This difference could be attributed to their greater burial depth and more intense compaction effects.

4.4.3. Pore Type

The observations reveal that the Wufeng–Longmaxi shale in the study area primarily contains organic matter pores, inorganic pores, and microfractures. Furthermore, there are certain differences in the type and degree of development of pores between deep and shallow shales. Organic matter pores developed within organic matter were usually formed during the processes of kerogen hydrocarbon generation and bitumen cracking [55]. Samples with a high TOC content usually have more developed organic matter, which is widely distributed between inorganic minerals in the form of clusters, stripes, or irregular shapes (Figure 8a,b). In some samples with a lower organic matter content, only sporadic organic matter fragments or irregularly shaped organic matter are observed, and organic matter pores are not developed (Figure 8b,c). Due to the high thermal maturity of kerogen, organic matter pores related to hydrocarbon generation and expulsion can be observed in most samples of the Longmaxi Formation (Figure 8d,h). These organic matter pores are mostly bubble-shaped or elliptical, and some densely developed small pores are interconnected to form large pores or more complex network systems, enhancing the heterogeneity (Figure 8e). Abundant, closely arranged, needle-like or honeycomb-shaped bitumen pores can also be observed in the bitumen (Figure 8f,g).

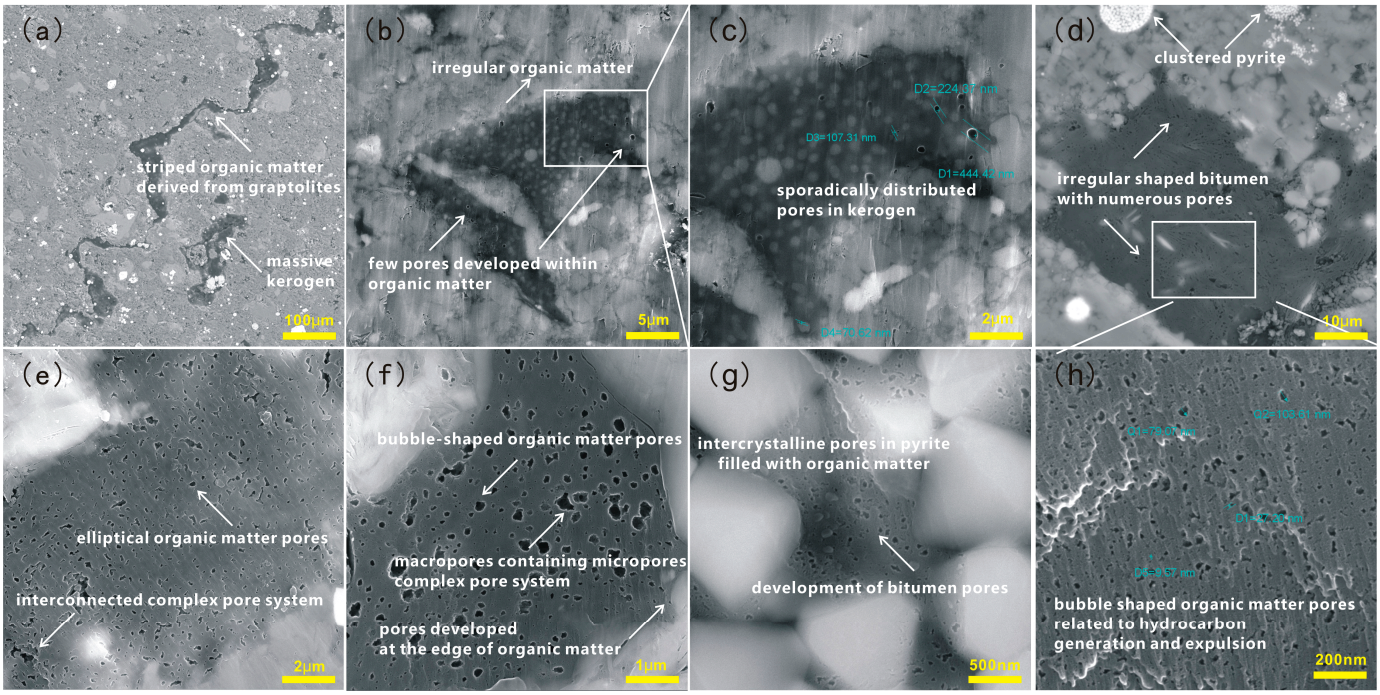

Figure 8. Characteristics of organic matter and organic matter pores in the Wufeng–Longmaxi shale. (**a**) Y11, TOC = 5.32%, R_o = 2.6%, striped organic matter derived from graptolites; (**b**) Y4, TOC = 0.96%, irregular-shaped organic matter; (**c**) is an enlarged image of (**b**), showing sporadically distributed pores in organic matter; (**d**) Y11, irregular-shaped bitumen with numerous organic matter pores; (**e**) Y9, TOC = 2.97%, R_o = 2.6%, elliptical-shaped organic matter pores; (**f**) L5, TOC = 2.59%, R_o = 2.46%, bubble-shaped organic matter pores, with small pores interconnected to form a complex pore network, and shrinkage fractures at the edges between organic matter and minerals; (**g**) L5, organic matter fills the interstitial pores between pyrite crystals and develops internal elliptical-shaped organic matter pores; and (**h**) is an enlarged image of (**d**), showing bubble-shaped organic matter pores related to hydrocarbon generation and expulsion.

Inorganic pores are the most important components of the shale reservoir space, and they mainly include intergranular pores and intragranular pores (Figure 9b). Their formation and preservation are controlled by multiple factors, such as the sedimentary environment, mineral composition, burial depth, diagenesis, and tectonic activity. Intergranular pores develop at the edges of mineral particles (Figure 9a), especially at the edges of minerals with the ability to resist compaction. Generally, intergranular pores tend to decrease with increasing burial depth [56]. Within or at the edges of clay minerals, there is a significant development of numerous sheet-like, layered, or irregularly shaped inorganic pores (Figure 9c,d). The diverse structures contribute to an increased specific surface area of shale, which is beneficial for gas adsorption. Intragranular pores mainly include intercrystalline pores and dissolution pores. The most typical intercrystalline pores observed in the study developed between clustered pyrite grains in argillaceous lamina-rich shale (Figure 9e,f), exhibiting angular shapes. Some of these pores may be filled with organic matter or other minerals (Figure 8g). Dissolution pores are formed by the dissolution of soluble minerals by corrosive fluids and are commonly found within feldspar and carbonate mineral particles in silty lamina-rich shale (Figure 9g). Microfractures are primarily distributed within or at the edges of mineral particles, often appearing as narrow cracks, serving as significant pathways for the migration of oil and gas. The widths of these fractures range from nanometers to micrometers, with lengths extending from a few micrometers to several hundred micrometers (Figure 9h,i).

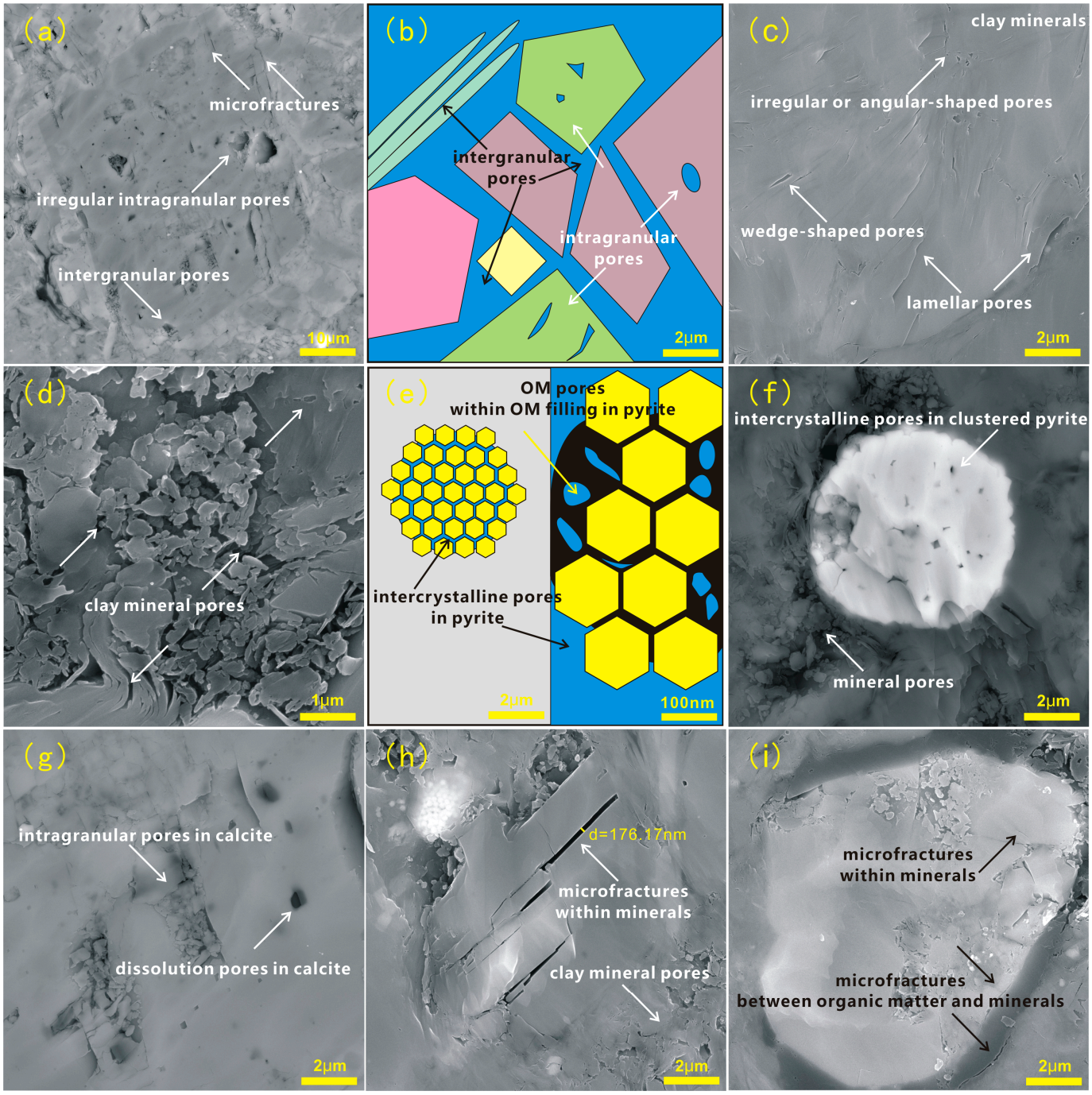

Figure 9. Characteristics of inorganic pores and microfractures in the Wufeng–Longmaxi shale. (**a**) L1, argillaceous/siliceous mixed shale, intergranular pores, intragranular pores and microfractures; (**b**) schematic diagram of intergranular pores and intragranular pores; (**c**) L8, clay mineral pores; (**d**) L4, mixed shale, with clay mineral pores; (**e**) schematic diagram of intercrystalline pores in pyrite and organic matter pores filled in pyrite; (**f**) L9, intercrystalline pores in clustered pyrite; (**g**) L1, dissolved pores in dolomite; (**h**) L12, microfractures within minerals; and (**i**) L5, microfractures developed along the edges between organic matter and minerals.

4.4.4. Pore Structure

Shale pore structure characterization includes the pore type, pore volume (PV), specific surface area (SSA), and pore size distribution (PSD). As shown in Figure 10a, the CO_2 adsorption capacity of argillaceous lamina-rich shale is generally greater than that of silty lamina-rich shale, indicating a larger micropore space. The N_2 adsorption–desorption isotherms of samples belong to type IV (Figure 10d), indicating the presence of both small pores and large pores. In its 2015 report, the IUPAC updated the classification of hysteresis loops, expanding H_1-H_4 types to H_1, $H_{2(a)}$, $H_{2(b)}$, H_3, H_4, and H_5 [57,58]. These types represent open cylindrical pores, ink bottle-shaped pores with narrow necks, ink bottle-shaped pores with wide necks, parallel plate-like pores, layered slit-like pores, and materials with partially blocked pores, respectively (Figure 10e). As shown in Figure 10b, the hysteresis loop of the argillaceous lamina-rich shale sample exhibits an $H_{2(b)}$-H_3-H_4 type, indicating the development of ink bottle-shaped and slit-shaped pores and suggesting a more complex pore structure. The hysteresis loop type of the silty lamina-rich shale is mainly H_3-H_4, with some adsorption–desorption curves almost overlapping and a narrow hysteresis loop. Plate-like and layered pores are conducive to gas adsorption and accumulation but are not favorable for gas permeation and diffusion. According to Chen et al.'s [14] classification scheme research (Figure 10f), the mercury intrusion curves of argillaceous lamina-rich shale mainly indicate type I and type II (Figure 10c). The initial stage of type I shows a convex or horizontal shape, indicating the development of small and medium pores. The significant volume difference between the intrusion–extrusion curve indicates a large number of open pores and good pore connectivity, which is conducive to the desorption, diffusion, and permeation of shale gas, representing favorable reservoirs for shale gas exploration and production. The mercury intrusion curves of the silty lamina-rich shale are mainly type II, indicating the development of a certain amount of open-type micropores in the pore system.

For the fine characterization of the shale pore structure, research combines gas adsorption and high-pressure mercury intrusion experimental test results through mathematical methods to obtain the pore size distribution curve (Figures 11a and 12). The results in Table 4 show that the average shale pore volumes in Well L, Well Y and Well N are 0.031509 cm^3/g, 0.025558 cm^3/g and 0.029146 cm^3/g, respectively. In shale samples, mesopores have the largest contribution to the total pore volume (51.3%), followed by micropores (21.4%) and macropores (27.3%) (Figure 11c). The average shale specific surface areas in in Well L, Well Y and Well N are 16.9580 m^2/g,18.7379 m^2/g and 15.2355 m^2/g, respectively. Different from the distribution of pore volume, micropores are the absolute contributor to the specific surface area (79.7%), followed by mesopores (20.1%). However, macropores can be neglected (0.2%) (Figure 11d).

In this study, the PSD pattern of shale reservoirs is shown by the incremental pore volume distribution curve (Figures 11b and 12). In Figure 12a, the PSD curve of argillaceous lamina-rich shale exhibits a bimodal distribution, with the main peaks occurring at 30 nm to 50 nm and 50,000 nm. The corresponding average pore volume increments are 0.0032 cm^3/g and 0.0044 cm^3/g, indicating that the range of large pore development is relatively concentrated. The small pores within the dashed line exhibit a multimodal distribution, suggesting that the range of small pore development is relatively dispersed. In Figure 12b, the silty lamina-rich shale exhibits a "nontypical" unimodal distribution, with the main peak position offset toward a larger pore size of 100,000 nm. The increment of pore volume is 0.0038 cm^3/g, including some microfractures. The small pores within the dashed line exhibit a bimodal pattern of development, with the main peaks occurring at 1.2 nm and 30 nm. The study found that, compared to the peak of large pores, the peaks of micropores and mesopores better reflect the degree of concentrated development within their respective pore size ranges. This is because the peak of large pores may be influenced by a few extremely developed pores. For example, the volume of a single large pore may be equivalent to the sum of the volumes of multiple small pores. Although they have the

same numerical value, the degree of pore development that they reflect can be different (Figure 11a).

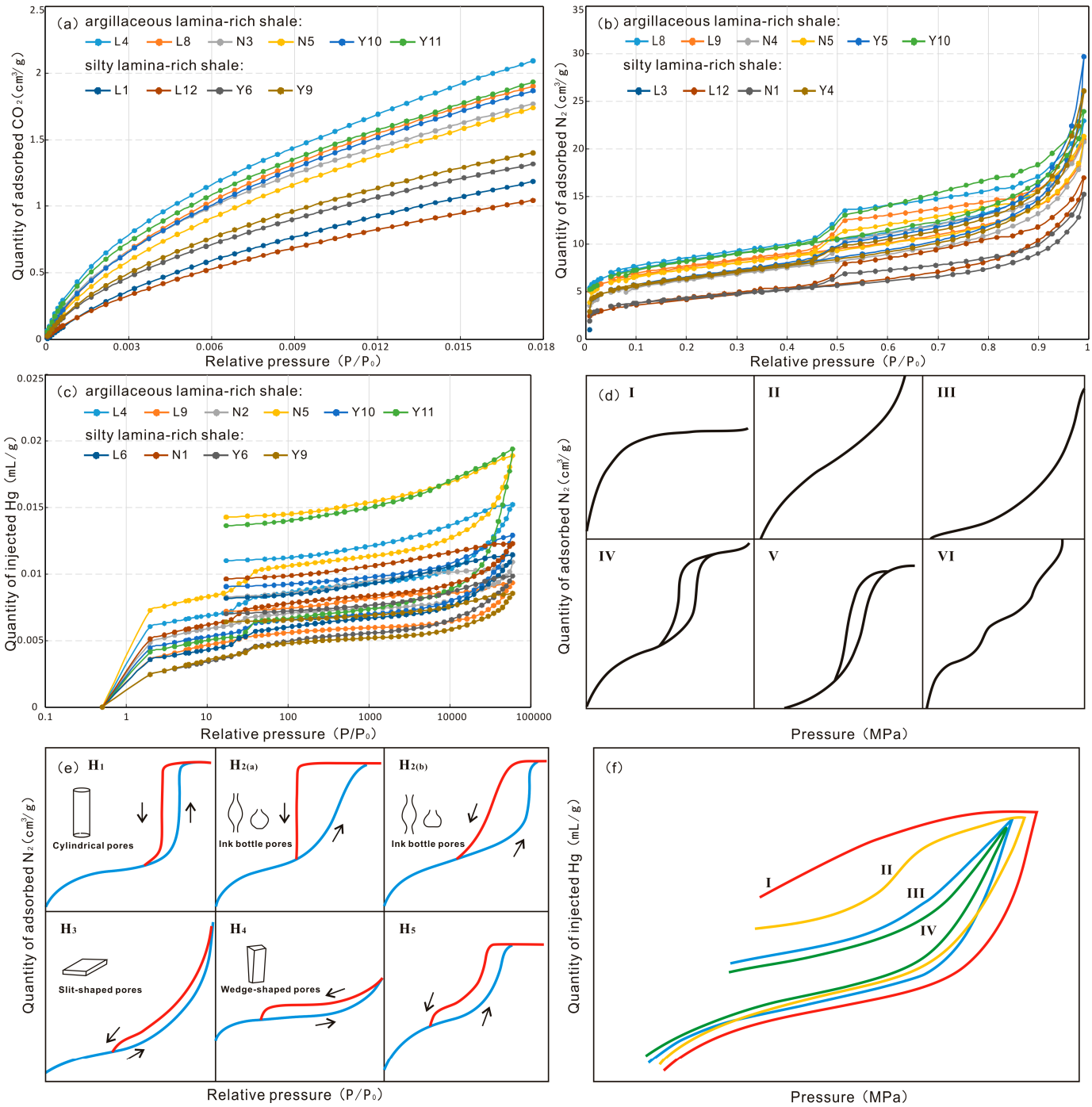

Figure 10. Gas adsorption and high-pressure mercury intrusion curves in the Wufeng–Longmaxi shale. (**a**) CO_2 adsorption curve; (**b**) N_2 adsorption–desorption curve; (**c**) mercury intrusion–extrusion curve; (**d**) classification of N_2 adsorption curves; (**e**) classification of the N_2 adsorption isotherm and hysteresis loops, modified from Thommess et al. [58]; and (**f**) classification of mercury intrusion curves, modified from Chen et al. [14].

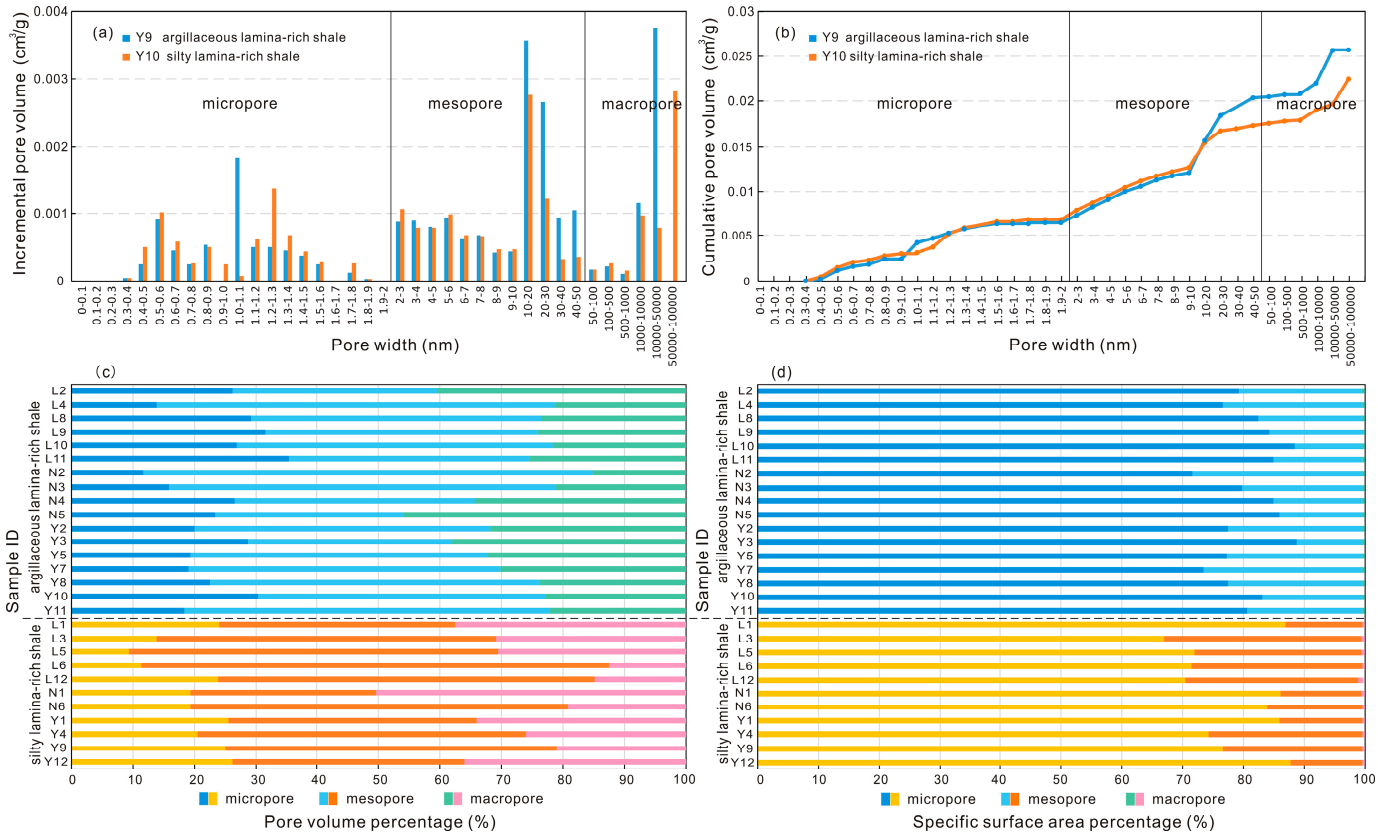

Figure 11. Pore structure differences between argillaceous lamina-rich shale and silty lamina-rich shale. (**a**) Incremental curves and (**b**) cumulative curves of pore volume, indicating that the pore volume of argillaceous lamina-rich shale is more developed; (**c**) development of pore volume and (**d**) specific surface area, with micropores and mesopores dominating.

Table 4. Micropore, mesopore, and macropore structure parameters of the Wufeng–Longmaxi Shale samples in the study area determined by gas adsorption and MICP techniques.

Sample	Stratum	Pore Volume (cm^3/g)				Specific Surface Area (m^2/g)				Average Diameter Calc. (nm) *
		Micro-	Meso-	Macro-	Total-	Micro-	Meso-	Macro-	Total-	
L1	Layer 7	0.004394	0.006970	0.006852	0.018216	9.7281	1.4156	0.0147	11.1584	13.06
L2	Layer 6	0.005169	0.006604	0.007954	0.019727	7.2450	1.8512	0.0202	9.1164	17.31
L3	Layer 6	0.001121	0.004450	0.002496	0.008067	1.8461	0.8937	0.0070	2.7468	23.49
L4	Layer 6	0.006312	0.029297	0.009684	0.045293	15.4559	4.6514	0.0238	20.1311	18.00
L5	Layer 5	0.005813	0.037259	0.019000	0.062072	14.8734	5.6982	0.0562	20.6278	24.07
L6	Layer 5	0.006395	0.042861	0.007027	0.056283	16.6959	6.5621	0.0223	23.2803	19.34
L7	Layer 4	0.006072	0.036185	0.002793	0.045050	15.8564	5.6636	0.0226	21.5426	16.73
L8	Layer 3	0.008359	0.013547	0.006744	0.028650	18.3527	3.8114	0.0173	22.1814	10.33
L9	Layer 2	0.008017	0.011194	0.006128	0.025339	17.2312	3.1563	0.0108	20.3983	9.94
L10	Layer 2	0.006741	0.012880	0.005427	0.025048	16.3583	2.0632	0.0143	18.4358	10.87
L11	Layer 1	0.009439	0.010365	0.006788	0.026592	21.0543	3.6673	0.0165	24.7381	8.60
L12	Wufeng	0.004251	0.010886	0.002631	0.017768	6.4607	2.5994	0.0786	9.1387	15.55
Y1	Layer 7	0.004286	0.006778	0.005712	0.016776	9.8072	1.5613	0.0129	11.3814	11.79
Y2	Layer 6	0.006863	0.016429	0.010876	0.034168	12.8901	3.6762	0.0286	16.5949	16.47
Y3	Layer 6	0.005306	0.006115	0.006999	0.018420	11.7375	1.4447	0.0076	13.1898	11.17
Y4	Layer 6	0.005335	0.013857	0.006762	0.025954	8.2890	2.8317	0.0193	11.1400	18.64
Y5	Layer 6	0.006653	0.016561	0.011081	0.034295	12.5641	3.6381	0.0292	16.2314	16.90
Y6	Layer 6	0.002756	0.016110	0.005919	0.024785	6.7489	2.5680	0.0228	9.3397	21.23
Y7	Layer 5	0.005673	0.015016	0.008963	0.029652	9.4504	3.3705	0.0245	12.8454	18.47
Y8	Layer 5	0.006994	0.016574	0.007369	0.030937	13.2551	3.7914	0.0173	17.0638	14.50
Y9	Layer 4	0.006448	0.013860	0.005416	0.025724	10.9667	3.2849	0.0145	14.2661	14.43
Y10	Layer 3	0.006825	0.010516	0.005154	0.022495	15.6228	3.0951	0.0200	18.7379	9.60
Y11	Layer 2	0.005503	0.017860	0.006686	0.030049	13.7423	3.2148	0.0370	16.9941	14.15
Y12	Wufeng	0.003528	0.005070	0.004839	0.013437	7.6098	1.0386	0.0059	8.6543	12.42
N1	Layer 5	0.003357	0.005250	0.008719	0.017326	7.7272	1.1955	0.0221	8.9448	15.50

Table 4. *Cont.*

Sample	Stratum	Pore Volume (cm^3/g)				Specific Surface Area (m^2/g)				Average Diameter Calc. (nm) *
		Micro-	Meso-	Macro-	Total-	Micro-	Meso-	Macro-	Total-	
N2	Layer 5	0.005889	0.036628	0.007631	0.050148	14.6001	5.7367	0.0147	20.3515	19.71
N3	Layer 4	0.005078	0.020105	0.006739	0.031922	12.6159	3.1105	0.0317	15.7581	16.21
N4	Layer 3	0.005409	0.007960	0.007014	0.020383	12.0128	2.0670	0.0194	14.0992	11.57
N5	Layer 3	0.006078	0.007982	0.012001	0.026061	13.6519	2.1651	0.0330	15.8500	13.15
N6	Layer 2	0.005625	0.017855	0.005558	0.029038	13.8196	2.5746	0.0153	16.4095	14.16

* Diameter Calc. = diameter calculated by Equation $(4V_p/A_s) \times 2$, where V_p = total pore volume of the shale, and A_s = total specific surface area of the shale.

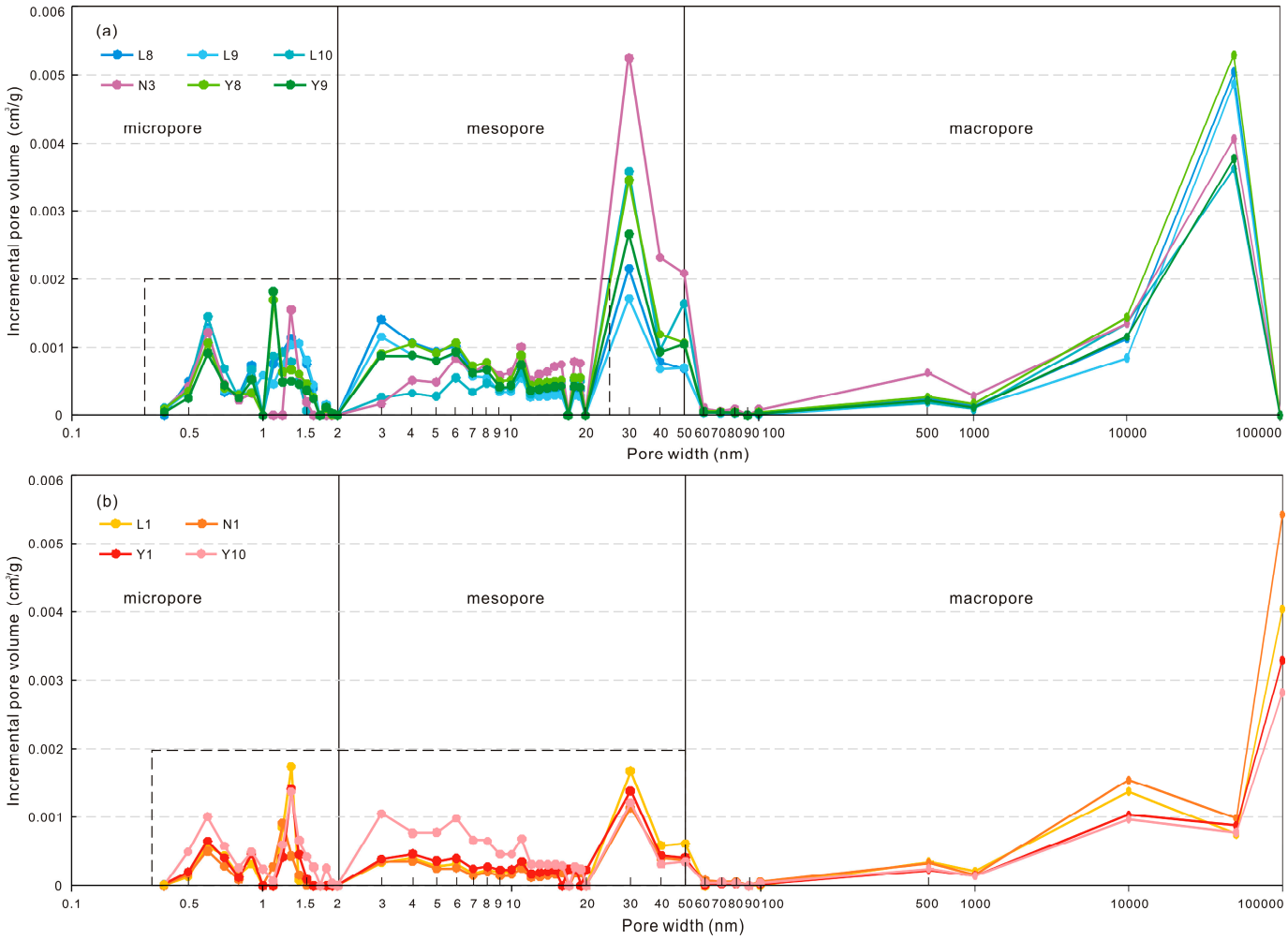

Figure 12. Pore size distribution differences between argillaceous lamina-rich shale and silty lamina-rich shale. (**a**) Pore size distribution of argillaceous lamina-rich shale, with a bimodal characteristic; (**b**) pore size distribution of silty lamina-rich shale, with a multimodal characteristic.

5. Discussion

5.1. Influence of Lamination on Shale Reservoir Properties

5.1.1. Comparison between Argillaceous Lamina-Rich Shale and Silty Lamina-Rich Shale

As mentioned in the Results, there are significant differences in hydrocarbon generation ability, pore development characteristics, and reservoir properties between argillaceous lamina-rich shale and silty lamina-rich shale. As shown in Figure 13a, the average TOC content of the argillaceous lamina-rich shale is 3.88%, which is higher than the 2.05% observed in the silty lamina-rich shale. High TOC content promotes the development of organic matter pores, which is beneficial for the adsorption and storage of shale gas. The average quartz content in argillaceous lamina-rich shale is 37.5%, which is significantly

higher than that of silty lamina-rich shale (with an average of 26.2%), indicating better fracturability. The average carbonate minerals content in silty lamina-rich shale is 30.3%, making it more prone to natural fracturing or dissolution. As shown in Figure 4b, the argillaceous lamina-rich shales have similar lithofacies types, with high silica content, while the lithofacies types of the silty lamina-rich shale are diverse.

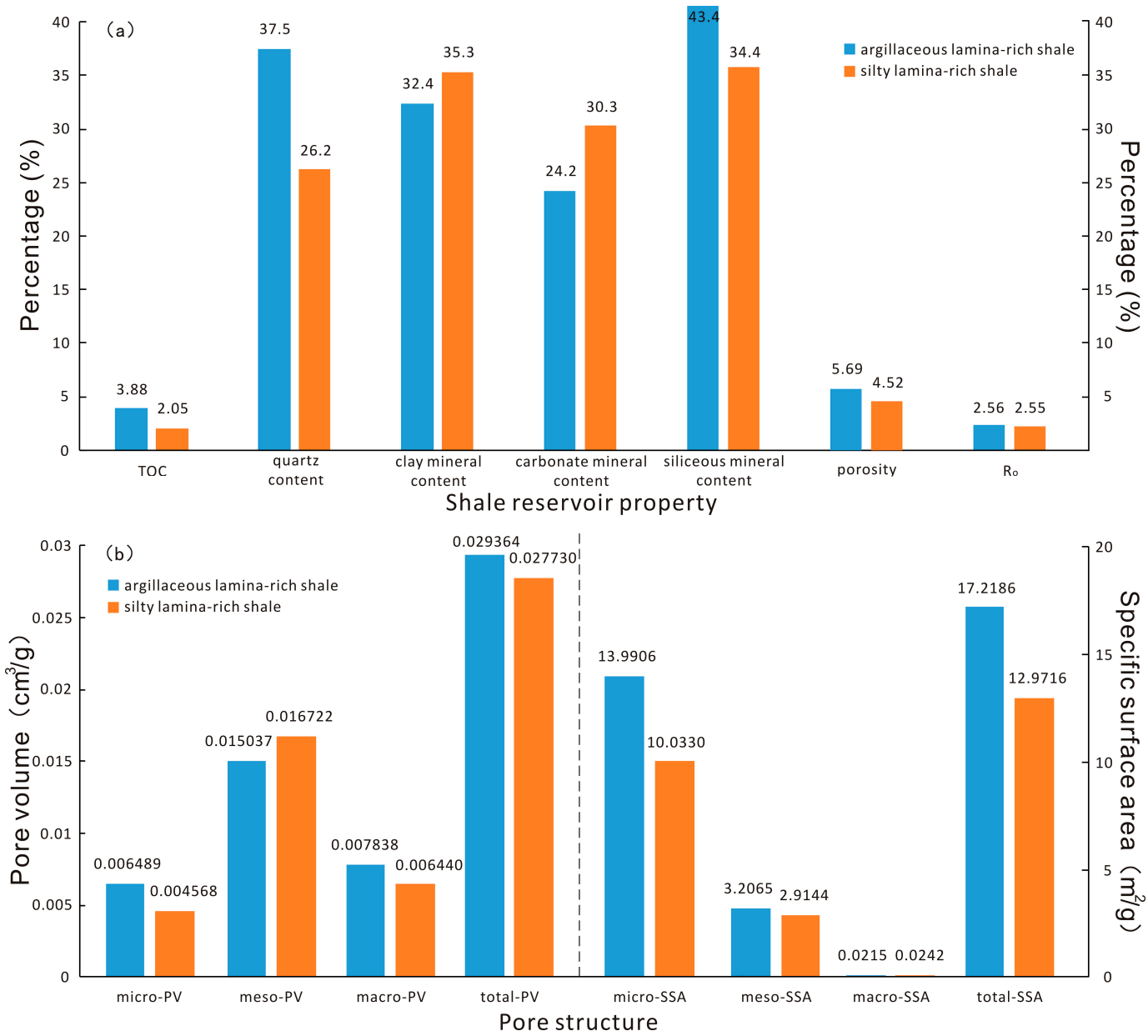

Figure 13. Comparison between argillaceous lamina-rich shale and silty lamina-rich shale in the study area. (**a**) Comparison of TOC, R_o, porosity and mineral composition; (**b**) comparison of pore volume and specific surface area.

The porosity of the argillaceous lamina-rich shale is higher than that of the silty lamina-rich shale. The porosities of the argillaceous lamina-rich shale in Layer 1~Layer 3 are generally greater than 6%, which may be related to their higher brittle mineral contents. The hysteresis loop of the argillaceous lamina-rich shale indicates the development of ink bottle-shaped and slit-shaped pores, suggesting a more complex pore structure. The mercury intrusion curve of the silty lamina-rich shale indicates the development of a certain amount of open-type micropores. The PV and SSA of argillaceous lamina-rich shale are generally larger than that of silty lamina-rich shale (Figure 13b). The PSD curve of argillaceous lamina-rich shale exhibits a bimodal distribution. The development range of large pores is relatively concentrated, while the development range of small pores is relatively dispersed. The PSD curve of silty lamina-rich shale exhibits a "nontypical" unimodal distribution. A large number of microfractures are developed in shale. Comparisons show that the argillaceous lamina-rich shales developed in anoxic reduction environments usually have higher TOC content, porosity, PV, SSA, and more developed organic matter pores. They have an improving effect on shale reservoir properties.

5.1.2. Main Factors Influencing the Development of Shale Pores

Factors such as the organic matter content, clay mineral composition, diagenesis, lithology and texture, tectonic activity, thermal history, and water saturation interact in complex ways and ultimately influence the storage and flow of fluids within shale reservoirs. Previous studies have shown that the TOC content and mineral composition are the most important factors influencing the shale pore structure. Shales with higher TOC and appropriate maturity tend to have more abundant and well-developed pores.

As shown in Figure 14a,c, the TOC content in samples from Wufeng–Longmaxi is positively correlated with micro-PV and micro-SSA, especially in Well L where the correlation coefficient exceeds 0.75 (Figure 14a). The TOC content also has a certain promoting effect on the meso-PV, total PV, and total SSA (Figure 14b,c). In contrast, TOC is not closely related to the development of macropores. Among the minerals, quartz, clay, and carbonate minerals have a more pronounced impact on the pore structure. The quartz content of the samples is negatively correlated with Zr, indicating that quartz is primarily of biogenic origin and is less influenced by terrigenous detritus. Quartz shows a positive correlation with TOC (Figure 14d), indicating a positive influence on pore development (Figure 14d–f). However, there is no correlation between clay and carbonate minerals and TOC, and there may even be a weak negative correlation ($R^2 < 0.1$). Clay minerals have a significant development of intergranular and intercrystalline pores, which play a promoting role in pore development. However, in this study, the correlation between the clay mineral content and pore volume is not high (Figure 14g). In addition to being influenced by shale heterogeneity, this result may also be related to the composition of clay minerals and diagenesis. The type and abundance of clay minerals in shales can affect pore development. Certain clay minerals, such as illite and chlorite, may contribute to the formation of interparticle or intercrystalline pores [11]. Diagenetic processes, including compaction, cementation, and fracturing, can significantly impact pore development in shales. Overburden pressure and mineral precipitation may reduce porosity [14]. This argument explains the observation that there is a low correlation between the clay mineral content and pore structure in deeply buried shale (Figure 14g,h), while there is a significant positive correlation between the clay mineral content and meso-PV and meso-SSA in shallowly buried shale (Figure 14g,h). The high content of carbonate minerals has an inhibitory effect on pore development (Figure 14i), indicating that the contribution of dissolution pores to pore structure is limited.

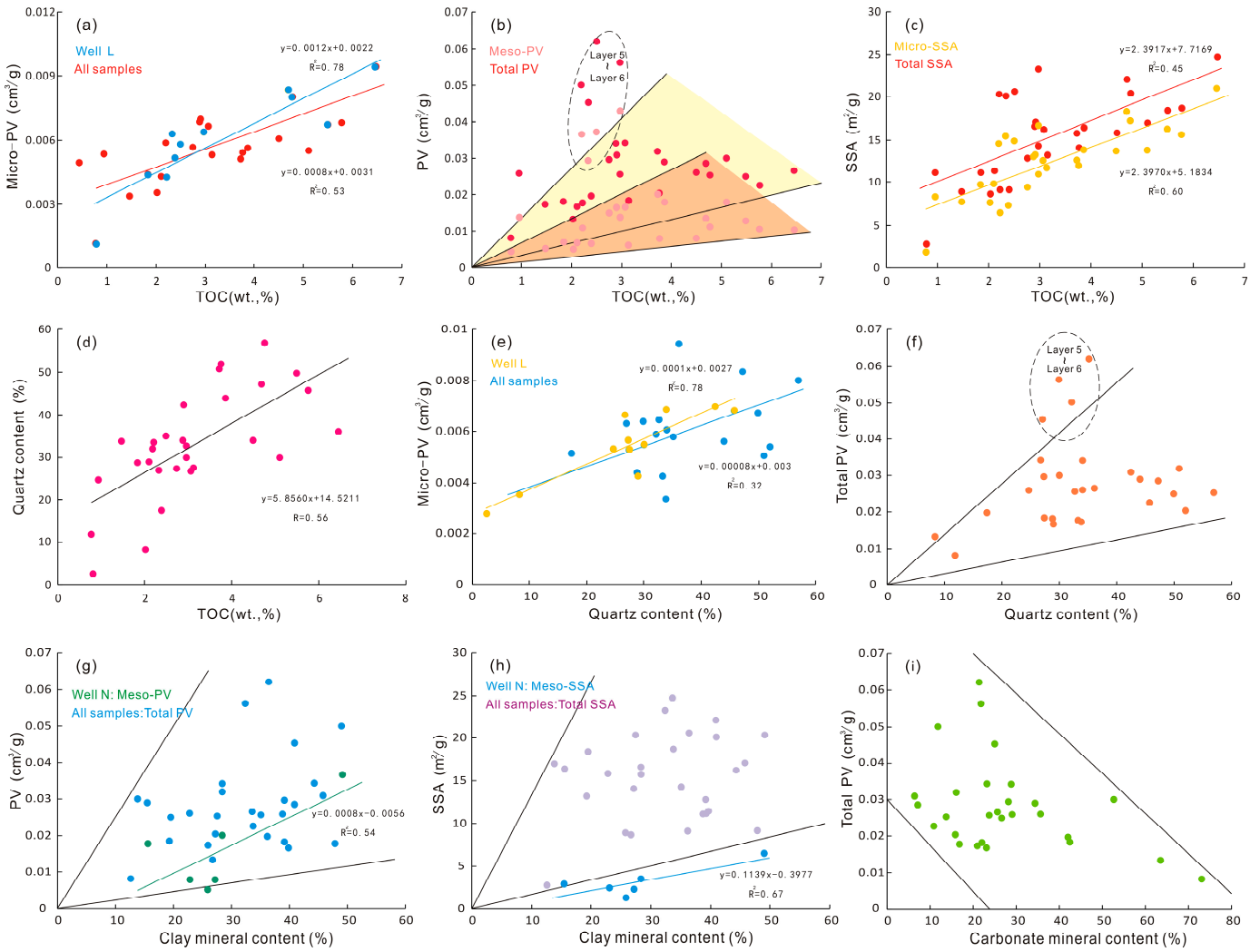

Figure 14. Relationships between the pore structure, TOC, and mineral composition of the Wufeng–Longmaxi shale in the study area. Images show a clear positive correlation between TOC and pore volume. The content of quartz and clay minerals has a promoting effect on pore structure. (**a**) Relationship between TOC content and micro-PV; (**b**) relationship between TOC content and PV; (**c**) relationship between TOC content and SSA; (**d**) relationship between TOC content and quartz content; (**e**) relationship between quartz content and micro-PV; (**f**) relationship between quartz content and total PV; (**g**) relationship between clay mineral content and PV; (**h**) relationship between clay mineral content and SSA; (**i**) relationship between carbonate mineral content and total PV.

5.2. Sedimentary Characteristics and Patterns of Variation

During the early deposition of the Longmaxi Formation, the entire Upper Yangtze region mainly developed deep-water shelf facies, characterized by black organic-rich shales. As the sedimentary environment transitioned from semideep-water shelf facies and shallow-water shelf facies to shoreline facies, the Longmaxi Formation gradually developed muddy sandstone, siltstone, and sandstone [59]. In this study, we used lithology and major and trace element analysis results to reconstruct the paleoredox conditions, water dynamic features, and productivity characteristics of the Wufeng–Longmaxi shale during deposition. During the sedimentation process, significant changes occurred in lamina characteristics and reservoir properties. To meet practical production requirements, this study further subdivided Layer 4 into Layer 4~Layer 7 based on the previous division by Zhu et al. [6].

The presence of abundant fossils from the Katian Stage to the Aeronian Stage in southern Sichuan makes the echinoderm zone an important marker for stratigraphic correlation and establishing geological correlations due to the high similarity in fossil assemblages among different areas [37]. However, the development of underwater ancient uplifts during the depositional period in certain areas resulted in thinning of high-quality shale and the absence of some graptolite zones (such as the WF1 graptolite zone) [2]. Compared to the Tiangongtang and Changning areas, the shale samples from the Luzhou area exhibit more complete variations in graptolites. This indicates that the stratigraphic development in this region is continuous and characterized by good stability, providing a comprehensive record for studying changes in sedimentary environments. Therefore, this study takes Well L as an example to demonstrate the sedimentary characteristics and variations in the Wufeng–Longmaxi shale in the southern Sichuan Basin (Figure 15).

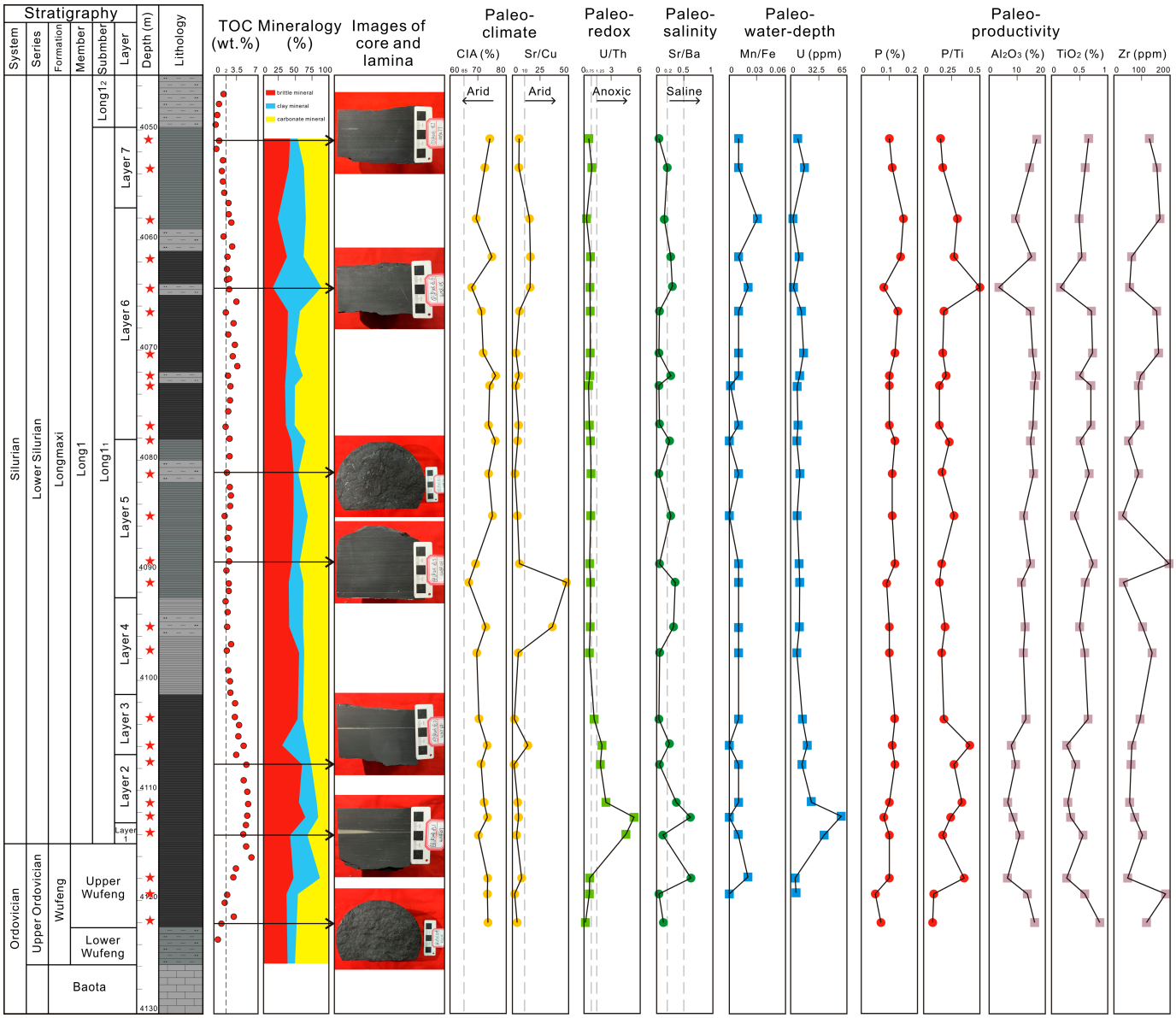

Figure 15. Changes in the sedimentary environment, lithology, and lamina characteristics of the Wufeng–Longmaxi shale in the Luzhou area.

(1) At the base of the Wufeng Formation (Pss1, WF1-2), U/Th < 0.75, indicating an oxic environment. The low U contents and Sr/Ba ratios (less than 0.2) suggest shallow water with low salinity. A low P content and P/Ti ratios indicate relatively low paleoproductivity. High levels of Al and Ti contents suggest a significant influence from detrital inputs. The lithology is predominantly gray–black silty mudstone without well-developed laminations. The core profile of the well Y sample reveals abundant banded pyrite, indicating significant disturbance (Figure 16a).

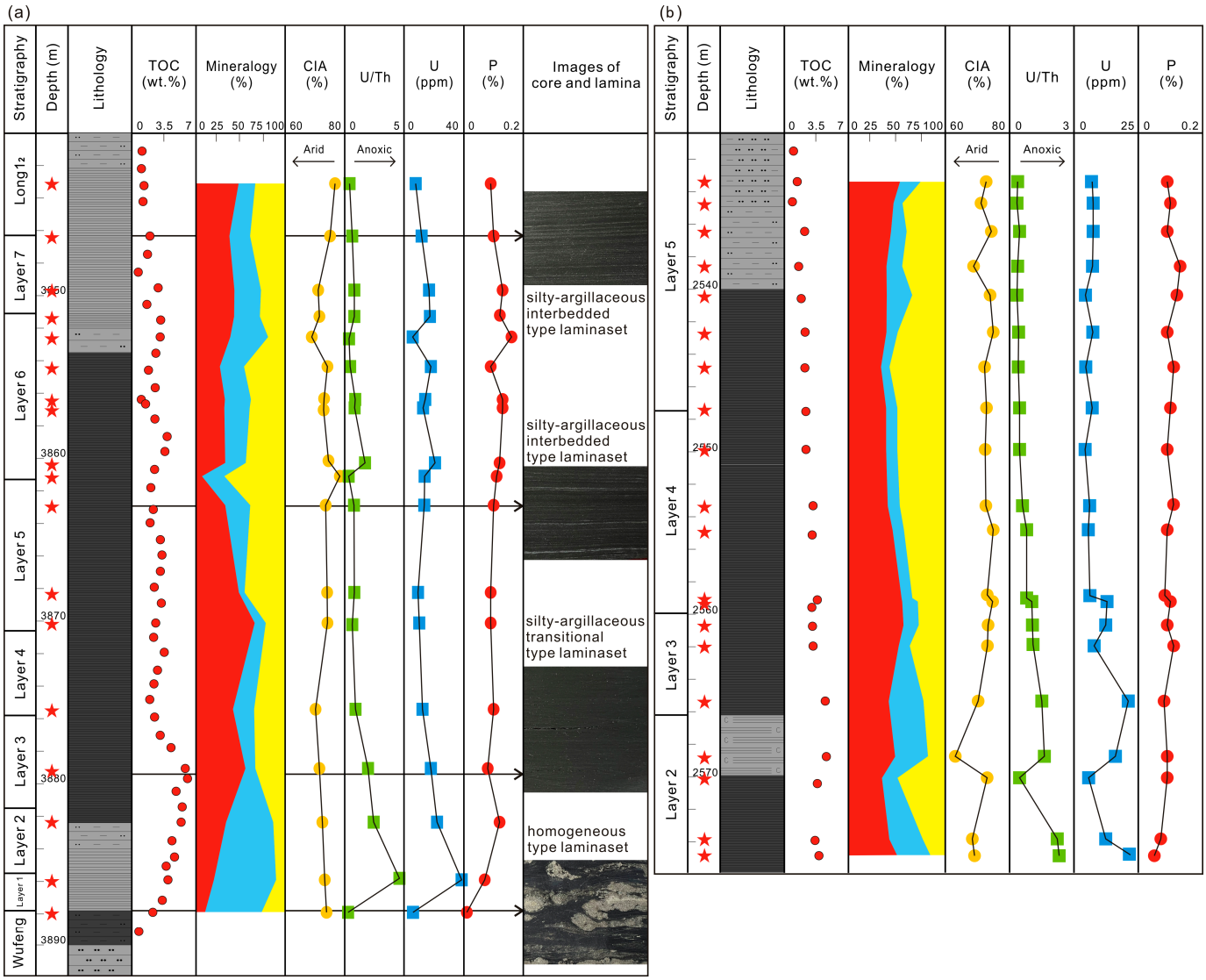

Figure 16. Changes in the sedimentary environment, lithology, and lamina characteristics of the Wufeng–Longmaxi shale in the Tiangongtang area (**a**) and Changning area (**b**).

(2) At the top of the Wufeng Formation (Pss2, WF3-4), U/Th = 0.6, which is slightly higher than the 0.35 observed at the base but still indicates an oxic environment. The slight increase in the U and P contents reflects the influence of the transition from glacial to interglacial conditions, indicating a gradual rise in sea level and enhanced paleoproductivity. At the top of the Wufeng Formation, a small number of initial thin laminae begin to develop, and the lithology consists of siliceous shale. The bentonite represents volcanic eruptions and indicates that some of the nutrient material comes from terrestrial sources, making them useful as stratigraphic markers [60]. In this study, no bentonite is observed, and there is a significant decrease in the Al and Ti contents. This suggests that the sedimentary environment in the study area after the first phase of large-scale transgression was

relatively stable and had minimal influence from terrestrial detrital inputs. The nutrient elements promoting biological proliferation in the surface water during this period may have originated from glacial meltwater injected by upwelling ocean currents [61].

(3) In Layer 1 (Pss3, LM1), the U/Th ratio rapidly increases to 4.67, indicating an extremely anoxic sedimentary environment with an enhanced degree of water retention. During the same period, the second biotic extinction event led to a significant decomposition of organisms, which consumed oxygen in the water. The U content abruptly increases from 4.8 (average value of Wufeng shales) to 38.6. This indicates that after the melting of the ice sheet, there was a significant rise in sea level, leading to an increase in the water depth. The P content slightly decreases but remains at a relatively high level. The combination of high paleoproductivity and an anoxic environment favors the enrichment of organic matter. The average TOC content in the black organic-rich shale reaches 6.5%. Laminations begin to develop in the shale, and spot-like or banded pyrite is observed in the core profile.

(4) In Layer 2 (Pss4, LM2-3), U/Th = 3.14, indicating an ongoing anoxic environment. The U content, P content, and P/Ti ratio remain stable, suggesting a deep-water depositional environment with high paleoproductivity. The Al and Ti contents are relatively low, indicating a relatively small influence from terrestrial detrital inputs. The lithology is mainly composed of black mixed siliceous shale and argillaceous-rich siliceous shale. The average TOC content is 5.2%, and the pyrite content is relatively high. Laminations in the core profile are well developed, mainly consisting of thin argillaceous laminae.

(5) In Layer 3 (Pss5, LM4-5), U/Th = 1.50, indicating an anoxic environment. The decrease in the U content suggests a decrease in sea level and a reduction in water retention. Microbial decomposition consuming a significant amount of oxygen led to water stratification. The P content and P/Ti ratio continue to increase, reaching their highest levels due to the dual nutrient supply from detrital input and glacial meltwater. The average TOC content in the argillaceous-rich siliceous shale is 4.8%. Compared to Layer 1~Layer 2, the shale exhibits lighter color, coarser grain size, and increased lamina thickness. Due to regional geological variations, the sedimentary environment of the shale in the Changning area had already started transitioning into a suboxic environment during this period (Figure 16b).

(6) In Layer 4 (Pss6, LM5-6), U/Th = 0.61, indicating a transition from an anoxic environment to a suboxic or oxic environment. The average U content decreases from 16.5 ppm in Layer 3 to 8.6 ppm, suggesting the end of large-scale marine transgression. The varying levels of paleoproductivity during the oscillating regression stages result in a decrease in the P content and P/Ti ratio. The elevated levels of Al and Ti indicate an increased input of terrestrial clastic material and an accelerated sedimentation rate. Some scholars propose that the favorable coupling of the "productivity mode" and "preservation mode" is a crucial factor for organic enrichment in shales. Under high sedimentation rates, oxygen-rich water can also lead to the deposition of organic-rich materials [3]. Layer 4 is primarily composed of black argillaceous-rich siliceous shale that exhibits well-developed laminations. The average TOC content is 2.4%, surpassing the lower threshold for organic richness needed for commercially exploitable shale gas deposits.

(7) In Layer 5 (Pss7, LM6), there is a slight increase in the U/Th ratio, U content, P content, and Al content, suggesting a minor-scale marine transgression. However, this does not significantly alter the overall sedimentary characteristics of the study area. It continues to exhibit a shallow-water, oxidized environment with moderate to high productivity. The lithology is predominantly gray and black argillaceous/siliceous mixed shale. The thicknesses of the laminae decrease, while their density increases.

(8) In Layer 6 (Pss7, LM7), there is an overall decrease in the U/Th ratio and U content, suggesting a minor decrease in the depth of oxygenated depositional water. Within Layer 6, the U content fluctuates between 2.6 ppm and 14.8 ppm, pointing to frequent fluctuations in sea level and an unstable sedimentary environment. The P and Al contents tend to stabilize, and the average TOC content remains at 2.4%. The lithology is mainly composed of black argillaceous-rich siliceous shale and gray–black argillaceous/siliceous mixed shale, with a reduction in the development of laminations and a more pronounced

interbedding of sand and mud. The bottom of Layer 6 is composed of black argillaceous-rich siliceous shale with a high content of pyrite. It gradually transitions upward to gray–black argillaceous/siliceous mixed shale and gray–white argillaceous/siliceous mixed calcareous shale. The development of lamination decreases, while the silty-argillaceous interbedded laminaset becomes more prominent.

(9) In Layer 7 (Pss8, LM8, no observation of LM9), there is a gradual decrease in the U/Th ratio and U content, indicating a shallowing of the depositional water. Due to the continuous input of terrestrial clastic material and the continuous consumption of algal matter, the lithology predominantly consists of argillaceous/siliceous mixed shale and silty mudstone in an oxygenated environment, with a TOC content lower than 2%. The development of laminations is indistinct.

Overall, the Wufeng Formation shale exhibits the greatest variation in elemental enrichment, indicating rapid changes in the depositional system. Layer 1~Layer 3 exhibit the highest TOC content, with organic matter presenting in striped, clumped, or irregular shapes, and a large number of organic pores developed internally. During the depositional period, the water depth was relatively deep, with a low oxygen content and weak water dynamic. Sedimentation is primarily dominated by suspended settling. Layer 4~Layer 5 exhibit a higher TOC content, an increased supply of terrestrial clastic material, and an increase in silt-sized particles. The depositional water became shallower during this period, with an enhanced oxygen content and water dynamic. The TOC content further decreases in Layer 6~Layer 7. The development of the interbedded silty-argillaceous type indicates an increase in the sedimentation rate and oxygen content, accompanied by a further increase in the supply of terrestrial clastic material. The paleowater dynamic conditions showed periodic changes.

5.3. Variations in Lamina and Laminaset and Their Relationship with the Depositional Environment

Previous studies have indicated that in a continental shelf depositional setting, laminae formation has occurred concurrently in areas such as Changning, Luzhou, Weiyuan, and western Chongqing [6]. Therefore, in the southern Sichuan region, the characteristics of laminae can serve as markers for stratigraphic comparison (Figures 15, 16a and 17c). From the perspective of laminae texture, the normally graded laminaset is related to turbidity currents or other sediment gravity flows. In contrast, the reverse graded laminaset is associated with turbulent flow, high suspended loads or periodic climate variations, while the homogenous laminaset is influenced by bioturbation and diagenetic processes [61]. From the perspective of the laminae structure, the laminae morphology is related to the hydraulic action and sedimentation mode [30]. Plate-like laminae form under conditions of strong unidirectional flow or settling in quiescent suspension, indicating a low water dynamic. Wavy laminae and curved laminae, on the other hand, indicate a higher water dynamic. The continuity and stacking relationship of laminae are related to the energy conditions of the water. Weak water dynamics tend to result in continuous laminae. A single flow direction and stable water dynamic are conducive to the formation of parallel laminae [62].

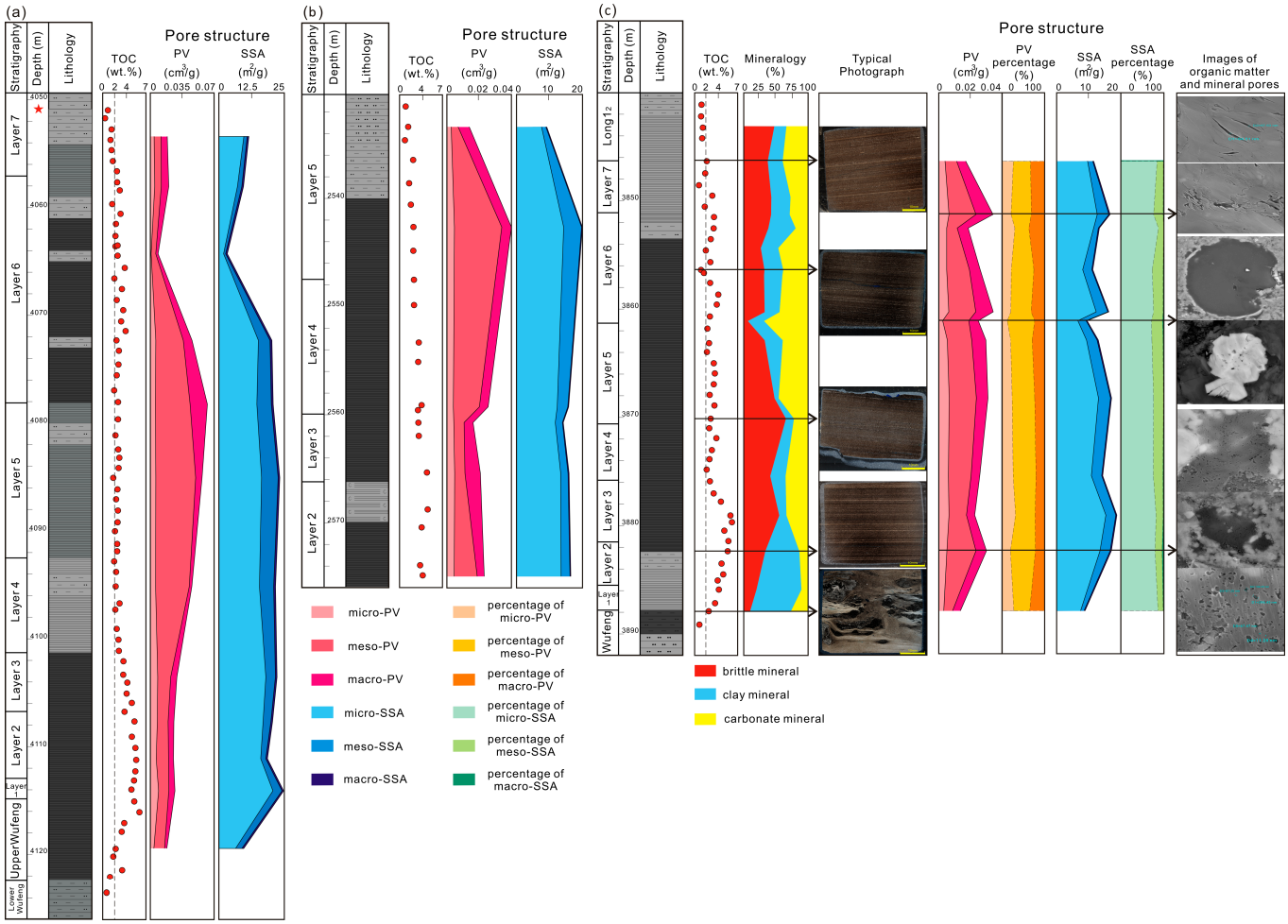

Figure 17. Characteristics of laminae development and pore structure of the Wufeng–Longmaxi shale in the study area. (**a**) Luzhou area and (**b**) Changning area, showing similar trend in pore structure changes, with larger pore volume in Layer 4~Layer 5; (**c**) Tiangongtang area shows the intermittent changes in the pore structure, as well as a promoting effect of argillaceous laminasets and organic matter pores on the pore volume.

(1) At the bottom of the Wufeng Formation, sedimentation is influenced by disturbances, and the water dynamic is relatively strong, resulting in the absence of laminae development. (2) Toward the top of the Wufeng Formation, discontinuous thin argillaceous laminae begin to develop, indicating a moderate level of water dynamic. (3) Layer 1 shows the gradual development of laminasets, primarily consisting of argillaceous laminasets with an average thickness of 0.30 cm, while the silty laminasets have an average thickness of 0.12 cm. (4) Layer 2 consists of argillaceous/carbonate mixed siliceous shale with well-developed laminae. The continuous parallel plate-like argillaceous laminasets dominate, with a higher density than that of Layer 1, indicating conditions of quiet water suspension settling and a relatively low paleowater dynamic. Organic laminae can be observed under microscopic examination, implying higher paleoproductivity conditions. (5) Layer 3 is characterized by argillaceous-rich siliceous shale and well-developed laminae. The thickness of both the argillaceous laminasets and silty laminasets increases. In the core profile, a normally graded laminaset can be identified. It occurs when sediments settle out of a fluid under decreasing energy conditions. Most of the laminae exhibit a continuous parallel plate-like distribution, with a few showing a discontinuous distribution, indicating a slightly enhanced water dynamic. (6) Layer 4 exhibits similar densities for both argillaceous laminasets and silty laminasets (3.25 stripes/cm and 3.50 stripes/cm, respectively), with the argillaceous laminasets being thicker. The interbedding between them becomes

more pronounced, with alternating bright and dark layers and clear interfaces (Figure 17). These changes are more evident in the Changning area (Figure 16b). The laminasets show a continuous parallel plate-like distribution, without any observed undulating or curving laminasets, indicating that although the sedimentary water becomes shallower, the energy of the water remains relatively low. (7) Layer 5 is primarily composed of argillaceous/siliceous mixed shale and exhibits developed laminae. The average thickness of the laminasets decreases, but argillaceous laminasets still dominate. The overall distribution of laminasets appear as continuous and parallel, with a slightly reduced degree of interbedding between argillaceous laminasets and silty laminasets. This indicates a decrease in the water dynamic and an increase in the water depth. (8) Layer 6 exhibits a noticeable decrease in laminaset thickness and a significant increase in density. In the upper section of Layer 6, the development of silty laminasets surpasses that of argillaceous laminasets. Some sample profiles show banded or clustered pyrite, indicating the occurrence of anoxic environments during this period. Microscopic observations reveal an increase in the quantity of calcareous laminae and a lower quantity of organic laminae, indicating accelerated sedimentation rates, increased input of terrestrial debris, and an enhanced water dynamic. (9) Layer 7 consists of argillaceous/siliceous mixed shale with relatively indistinct laminae development. It is primarily characterized by continuous parallel silty laminasets, with occasional discontinuous parallel laminasets, indicating further enhancement of water dynamic characteristics.

Overall, the type of laminaset transitions from a homogeneous type at the base of the Wufeng Formation to a silty-argillaceous transitional type in Layer 2~Layer 3 and then to a silty-argillaceous interbedded type in Layer 5~Layer 7 (Figure 15). The argillaceous laminae are developed throughout the entire sedimentary process, with a large thickness and good continuity in Layers 1–3. They trend to form in reducing environments characterized by deeper water bodies, a lower water dynamic, less input of terrestrial detritus, and low oxygen levels, while as the sedimentary environment transitioned from an anoxic environment into a suboxic or oxic environment, the silty laminae gradually developed and interbedded with the argillaceous laminae. It can be concluded that the sedimentary environment significantly affects the type, development degree, and development characteristics of laminae.

5.4. Pore Structure and Its Relationship with the Depositional Environment and Lamination

Laminae are distinctive sedimentary structures widely developed in the shale of Wufeng–Longmaxi Formation, which enhances the heterogeneity of the reservoir. They can not only control the pattern of fracture propagation and the effectiveness of hydraulic fracturing, but also influence the hydrocarbon generation capacity and the microstructure of shale [25]. As discussed in Section 5.1.2, pore volume is mainly influenced by TOC content and mineral composition, which are closely related to the sedimentary environment and diagenesis. High TOC content, clay content, and quartz content are beneficial for the development and preservation of organic matter pores and mineral pores, increasing the porosity and PV of shale reservoir. At the same time, the argillaceous lamina-rich shale developed in anoxic environments are characterized by high TOC content and high siliceous minerals, indicating a certain coupling relationship between sedimentary environment, lamination, and pore structure. By analyzing the development characteristics and variation patterns of laminations, the sedimentary environment and reservoir properties of shale can be determined.

As shown in Figure 17, the PV and SSA exhibit an intermittent fluctuating trend with changes in the sedimentary environment. The shales developed in Layer 2~Layer 3 exhibit high micro-PV and significant SSA values. The shales in the upper part of Layer 4 to Layer 5 generally have larger pore volumes. However, the pore volume of shales developed in Layer 6 decreased with sedimentation, while the shales in Wufeng and Layer 7 have the smallest pore volumes. Analyzing the sedimentary environment and lithology, it can be inferred that during the deposition of Layer 2~Layer 3, there was

a greater water depth, lower oxygen content, higher paleoproductivity, weaker water dynamic, finer sediment particles, and a large number of argillaceous laminae, resulting in a more compact deposition. A high TOC content is conducive to the development of organic matter pores and increases the micro-PV, while higher clay content reduces the shale's ability to resist compaction, leading to deformation or closure of some mineral pores during diagenesis. During the deposition of Layer 4~Layer 5, there was a shallower water depth, higher oxygen content, stronger water dynamic, coarser sediment particles, and relatively chaotic deposition. The moderate clay mineral content and relatively weak diagenesis enabled better preservation of pores, resulting in a significant increase in the mesopore volume. This phenomenon also indicates that the reservoir properties of the silty-argillaceous transitional type with moderate development of silty laminae are better than those of the pure argillaceous type, and homogeneous type.

Furthermore, statistical results indicate that the pore volume, specific surface area, and porosity of the argillaceous lamina-rich shale in the study area are generally greater than those of the silty lamina-rich shale (Figure 13). According to Shi et al. [28], an important distinction between argillaceous lamina-rich shale and silty lamina-rich shale is that the former exhibits a significantly higher quartz content, while the latter has a higher content of carbonate minerals. In argillaceous lamina-rich shale, quartz enhances its compressive strength and helps protect the surrounding primary pores from closure due to compaction. During the deposition of argillaceous lamina-rich shale, there was a greater water depth, lower oxygen content, higher paleoproductivity, and weaker water dynamic. The abundant parent material source, appropriate sedimentation rate, and higher content of brittle minerals facilitated the enrichment of organic matter and preservation of pores. In contrast, silty lamina-rich shale represents an open environment with strong water dynamic and a high oxygen content. The input of terrestrial clastics and increased content of carbonate minerals are unfavorable for the generation and preservation of pores. Overall, argillaceous lamina-rich shale and the anoxic sedimentary environment it represents have a positive impact on improving the shale pore structure and enhancing reservoir properties.

6. Conclusions

(1) The shale of the Wufeng–Longmaxi Formation has high TOC content, an advanced maturity stage and strong hydrocarbon generation ability. A large number of elliptical or bubble-shaped organic matter pores have developed within the kerogen and bitumen, promoting the development of micropore and mesopore. The development of intragranular pores, intergranular pores, and microfractures in minerals provides abundant space for the storage and migration of shale gas. Compared to shallow shale, deep shale has undergone stronger diagenesis, resulting in lower porosity and stronger reservoir heterogeneity.

(2) The Wufeng Formation was deposited in a suboxic to oxic environment, with shallow water depth, high oxygen content and weak productivity. Affected by strong water dynamic and biological disturbance, there is almost no development of laminae. The TOC content and pore volume of shale are smaller than those of the Longmaxi Formation shale. In the Longmaxi Formation, from Layer 1 at the base to the Layer 7 at the top, the sedimentary environment changed from anoxic to suboxic and oxic, the water depth gradually decreased, and the energy of water bodies and the input of terrigenous clastic material gradually increased, while the ancient productivity remained at a relatively high level. As a result, thick laminated organic-rich shale was deposited.

(3) The dark argillaceous laminae are mainly deposited in environments characterized by anoxic, deep water, unidirectional water flow and weak water dynamic, with most of them exhibiting continuous, parallel, and plate-like distributions. By analyzing the development characteristics, the sedimentary environment and reservoir properties of shale can be determined. Compared with light silty lamina-rich shale, the argillaceous lamina-rich shale has higher contents of TOC, porosity, quartz and clay minerals, larger pore volume and specific surface area, and more developed organic matter pores, which can improve shale reservoir properties.

(4) Vertically, the silty lamina increases from Layer 4, indicating an increase in the water dynamic and changing the stacking relationship between laminae. The silty-argillaceous transitional type mainly developed in Layer 2~Layer 3 and is characterized by a normally graded laminaset. The silty-argillaceous interbedded type developed in Layer 4~Layer 7, with clear boundaries and distinct variations. The pore volume of shales in Layer 4~Layer 5 with moderate development of silty laminae is larger than that of pure argillaceous type shale and homogeneous type shale, indicating that the sedimentary environment and laminae development have an important impact on reservoir properties.

Author Contributions: Conceptualization, X.M. and J.T.; methodology, X.M. and J.T.; software, J.X.; validation, X.M., H.W. and Y.W.; formal analysis, X.M.; investigation, X.M.; resources, J.T.; data curation, W.L.; writing—original draft preparation, X.M.; writing—review and editing, X.M.; visualization, X.M.; supervision, J.T.; project administration, J.T.; funding acquisition, J.T. All authors have read and agreed to the published version of the manuscript.

Funding: This research was funded by Science and Technology Bureau, Changsha, China, grant number [kq2208261].

Data Availability Statement: No new data were created.

Acknowledgments: We would like to thank all the editors and reviewers for their constructive comments on this paper.

Conflicts of Interest: The authors declare no conflicts of interest.

References

1. Liao, C.J.; Chen, L.; Zheng, J.; Chen, Y.N.; Jin, Z.M.; Li, M.L.; Chen, X.; Tan, X.C. Classification of shale lithofacies from Ordovician Wufeng Formation to first section of first member of Silurian Longmaxi Formation, western Changning area, Sichuan Basin, and its significance. *Pet. Geol. Exp.* **2022**, *44*, 1037–1047. [CrossRef]
2. Ma, X.H.; Xie, J. The progress and prospects of shale gas exploration and exploitation in southern Sichuan Basin, NW China. *Pet. Explor. Dev.* **2018**, *45*, 161–169. [CrossRef]
3. Pu, B.L.; Dong, D.Z.; Wang, F.Q.; Wang, Y.M.; Huang, J.L. The effect of sedimentary facies on Longmaxi shale gas in southern Sichuan Basin. *Geol. China* **2020**, *47*, 111–120. [CrossRef]
4. Wang, H.Y.; Shi, Z.S.; Sun, S.S. Biostratigraphy and reservoir characteristics of the Ordovician Wufeng Formation-Silurian Longmaxi Formation shale in the Sichuan Basin and its surrounding areas, China. *Pet. Explor. Dev.* **2021**, *48*, 1019–1032. [CrossRef]
5. Yang, X.; Shi, X.W.; Zhu, Y.Q.; Liu, J.; Li, Y.; He, L.; Xu, L.; Li, Y.Y.; Chen, Y.; Jiang, J.Y. Sedimentary evolution and organic matter enrichment of Katian-Aeronian deep-water shale in Luzhou area, southern Sichuan Basin. *Acta Pet. Sin.* **2022**, *43*, 469–482. [CrossRef]
6. Zhu, Y.Q.; Chen, G.S.; Liu, Y.; Shi, X.W.; Wu, W.; Luo, C.; Yang, X.; Yang, Y.R.; Zou, Y.H. Sequence stratigraphy and lithofacies paleogeographic evolution of Katian Stage–Aeronian Stage in southern Sichuan Basin, SW China. *Pet. Explor. Dev.* **2021**, *48*, 1126–1138. [CrossRef]
7. Zhang, J.C.; Tao, J.; Li, Z.; Wang, X.W.; Li, X.Q.; Jiang, S.L.; Wang, D.S.; Zhao, X.X. Prospect of deep shale gas resources in China. *Nat. Gas Ind.* **2021**, *41*, 15–28. [CrossRef]
8. Ma, X.H.; Xie, J.; Yong, R.; Zhu, Y.Q. Geological characteristics and high production control factors of shale gas reservoirs in Silurian Longmaxi Formation, southern Sichuan Basin, SW China. *Pet. Explor. Dev.* **2020**, *47*, 901–915. [CrossRef]
9. Algeo, T.J.; Kuwahara, K.; Sano, H.; Bates, S.; Lyons, T.; Elswick, E.; Hinnov, L.; Ellwood, B.; Moser, J.; Maynard, J.B. Spatial variation in sediment fluxes, redox conditions, and productivity in the Permian-Triassic Panthalassic Ocean. *Palaeogeogr. Palaeoclimatol. Palaeoecol.* **2011**, *308*, 65–83. [CrossRef]
10. Gao, P.; Liu, G.D.; Jia, C.Z.; Yong, A.; Wang, Z.C.; Wang, T.S.; Zhang, P.W.; Wang, D.P. Redox variations and organic matter accumulation on the Yangtze carbonate platform during late Ediacaran-early Cambrian: Constraints from petrology and geochemistry. *Palaeogeogr. Palaeoclimatol. Palaeoecol.* **2016**, *450*, 91–110. [CrossRef]
11. Chen, S.B.; Qin, Y.; Wang, Y.; Zhang, H.; Zuo, Z.X. Pore structure and heterogeneity of marine shales in the Middle-Upper Yangtze. *Nat. Gas Geosci.* **2015**, *26*, 1455–1463. [CrossRef]
12. Chalmers, G.R.; Bustin, R.M.; Power, I.M. Characterization of gas shale pore systems by porosimetry, pycnometry surface area, and field emission scanning electron microscopy/transmission electron microscopy image analyses: Examples from the Barnett, Woodford, Haynesville, Marcellus, and Doig units. *AAPG Bull.* **2012**, *96*, 1099–1119. [CrossRef]
13. Loucks, R.G.; Reed, R.M.; Ruppel, S.C.; Jarvie, D.M. Morphology, genesis, and distribution of nanometer-scale pores in siliceous mudstones of the Mississippian Barnett Shale. *J. Sediment. Res.* **2009**, *79*, 848–861. [CrossRef]
14. Chen, S.B.; Xia, X.H.; Qin, Y.; Fu, C.Q.; Hu, L. Classification of pore structures in shale gas reservoir at the Longmaxi Formation in the south of Sichuan Basin. *J. China Coal Soc.* **2013**, *38*, 760–765. [CrossRef]

15. Slatt, E.M.; O'Brien, N.R. Pore types in the Barnett and Wood-ford gas shales: Contribution to understanding gas storage and migration pathways in fine-grained rocks. *AAPG Bull.* **2011**, *95*, 2017–2030. [CrossRef]
16. Loucks, R.G.; Reed, R.M.; Ruppel, S.C.; Hammes, U. Spectrum of pore types and networks in mudrocks and a descriptive classification for matrix-related mudrock pores. *AAPG Bull.* **2012**, *96*, 1071–1098. [CrossRef]
17. IUPAC (International Union of Pure and Applied Chemistry). Physical chemistry division commission on colloid and surface chemistry, subcommittee on characterization of porous solids: Recommendations for the characterization of porous solids (Technical report). *Pure Appl. Chem.* **1994**, *66*, 1739–1758. [CrossRef]
18. Wang, Y.R.; Hu, Z.Q.; Dong, L.; Gao, B.; Sun, C.X.; Yang, T.; Wang, G.P.; Yin, S. Advancement and trends of shale gas reservoir characterization and evaluation. *Oil Gas Geol.* **2021**, *42*, 54–65. [CrossRef]
19. Li, Y.; Yang, J.H.; Pan, Z.J.; Tong, W.S. Nanoscale pore structure and mechanical property analysis of coal: An insight combing AFM and SEM images. *Fuel* **2020**, *260*, 116352. [CrossRef]
20. Clarkson, C.R.; Solano, N.R.; Bustin, R.M.; Bustin, A.M.M.; Chalmers, G.R.L.; He, L.; Melnichenko, Y.B.; Radlinski, A.P.; Blach, T.P. Pore structure characterization of North American shale gas reservoirs using USANS/SANS, gas adsorption, and mercury intrusion. *Fuel* **2013**, *103*, 606–616. [CrossRef]
21. Ma, X.; Guo, S.; Shi, D.; Zhou, Z.; Liu, G.H. Investigation of pore structure and fractal characteristics of marine-continental transitional shales from Longtan Formation using MICP, gas adsorption, and NMR (Guizhou, China). *Mar. Pet. Geol.* **2019**, *107*, 555–571. [CrossRef]
22. Hu, Q.H.; Liu, H.M.; Li, M.W.; Li, Z.; Yang, R.; Zhang, Y.X.; Sun, M.D. Wettability, pore connectivity and fluid-tracer migration in shale oil reservoirs of Paleogene Shahejie Formation in Dongying sag of Bohai Bay Basin, East China. *Acta Pet. Sin.* **2018**, *39*, 278–289. [CrossRef]
23. Ma, X.; Guo, S.B. Study on pore evolution and diagenesis division of a Permian Longtan transitional shale in Southwest Guizhou, China. *Energy Sci. Eng.* **2020**, *9*, 58–79. [CrossRef]
24. Lin, C.M.; Wang, H.Y.; Liang, P.P.; Shi, Z.S.; Sun, S.S.; Liu, D.X. The characteristics of laminae and its reservoir significance in black shale: Taking the Wufeng-Longmaxi formations in the Changning-Shuanghe section as an example. *J. Stratigr.* **2019**, *43*, 133–140. [CrossRef]
25. Xi, K.L.; Li, K.; Cao, Y.C.; Lin, M.R.; Niu, X.B.; Zhu, R.K.; Wei, X.Z.; You, Y.; Liang, X.W.; Feng, S.B. Laminae combination and shale oil enrichment patterns of Chang 73 sub-member organic-rich shales in the Triassic Yanchang Formation, Ordos Basin, NW China. *Pet. Explor. Dev.* **2020**, *47*, 198–209. [CrossRef]
26. Shi, Z.S.; Dong, D.Z.; Wang, H.Y.; Sun, S.S.; Wu, J. Reservoir characteristics and genetic mechanisms of gas-bearing shales with different laminae and laminae combinations:A case study of Member 1 of the Lower Silurian Longmaxi shale in Sichuan Basin, SW China. *Pet. Explor. Dev.* **2020**, *47*, 829–840. [CrossRef]
27. Hua, G.L.; Wu, S.T.; Qiu, Z.; Jiang, Z.H.; Xu, J.L.; Guan, M.D. Lamination Texture and Its Effect on Reservoir Properties: A Case Study of Longmaxi Shale, Sichuan Basin. *Acta Sedimentol. Sin.* **2021**, *39*, 281–296. [CrossRef]
28. Shi, Z.; Qiu, Z.; Dong, D.; Lu, B.; Liang, P.P.; Zhang, M.Q. Lamina characteristics of gas-bearing shale fine-grained sediment of the Silurian Longmaxi Formation of Well Wuxi 2 in Sichuan Basin, SW China. *Pet. Explor. Dev.* **2018**, *45*, 358–368. [CrossRef]
29. Aplin, A.C.; Macquaker, J.H.S. Mudstone diversity: Origin and implications for source, seal, and reservoir properties in petroleum systems. *AAPG Bull.* **2011**, *95*, 2031–2059. [CrossRef]
30. Lazar, O.R.; Bohacs, K.M.; Macquaker, J.H.S.; Schieber, J.; Demko, T.M. Capturing key attributes of fine-grained sedimentary rocks in outcrops, cores, and thin sections: Nomenclature and description guidelines. *J. Sediment. Res.* **2015**, *85*, 230–246. [CrossRef]
31. Guo, L.; Feng, C.J.; Guo, F. *Sedimentary Environment and Sedimentary Facies of Fine-Grained Rock Reservoirs-Taking Longmaxi Formation in the Southeast of Sichuan Basin as an Example*; Sinopec Press: Beijing, China, 2017; pp. 1–213.
32. Wo, Y.J.; Xiao, K.X.; Zhou, Y.; Yang, Z.Q. Types of marine plays in southern China and exploration prospects. *Oil Gas Geol.* **2006**, *27*, 11–16. [CrossRef]
33. Lu, Y.B.; Hao, F.; Lu, Y.C.; Yan, D.T.; Xu, S.; Shu, Z.G.; Wang, Y.X.; Wu, L.Y. Lithofacies and depositional mechanisms of the Ordovician-Silurian Wufeng-Longmaxi organic-rich shales in the Upper Yangtze area, southern China. *AAPG Bull.* **2020**, *104*, 97–129. [CrossRef]
34. Wang, Y.W. *Deep Shale Reservoir Characteristics of Wufeng-Longmaxi Formation in Luzhou Block*; China University of Mining and Technology: Xuzhou, China, 2023. [CrossRef]
35. Li, J.; He, D.F.; Mei, Q.H. Tectonic-depositional environment and proto-type basins evolution of the Ordovician in Sichuan Basin and adjacent area. *Acta Pet. Sin.* **2015**, *36*, 427–445. [CrossRef]
36. Feng, Z.Z. Discussion on petroleum exploration of marine strata South China from quantitative lithofacies palaeogeography. *J. Palaeogeogr.* **2005**, *7*, 1–11. [CrossRef]
37. Chen, X.; Fan, J.X.; Zhang, Y.D.; Wang, H.Y.; Chen, Q.; Wang, W.H.; Liang, F.; Guo, W.; Zhao, Q.; Nie, H.K.; et al. Subdivision and delineation of the Wufeng and lungmachi black shales in the subsurface areas of the Yangtze platform. *J. Stratigr.* **2015**, *39*, 351–358. [CrossRef]
38. Qiu, Z.; Dong, D.Z.; Lu, B.; Zhou, J.; Shi, Z.S.; Wang, H.Y.; Lin, W.; Zhang, C.C.; Liu, D.X. Discussion on the relationship between graptolite abundance and organic enrichment in shales from the Wufeng and Longmaxi Formation, South China. *Acta Sedimentol. Sin.* **2016**, *34*, 1011–1020. [CrossRef]

39. Zhao, S.X.; Yang, Y.M.; Zhang, J.; Wang, L.S.; Wang, X.Z.; Luo, C.; Tian, C. Micro-layers division and fine reservoirs contrast of Lower Silurian Longmaxi Formation shale, Sichuan Basin, SW China. *Nat. Gas Geosci.* **2016**, *27*, 470–487. [CrossRef]
40. Luo, C.; Li, J.X.; Li, Z.W.; Zhang, D.J.; Tong, K.L.; Dai, Y.; Hu, X.; Liu, A.D.; Ye, Y.H.; Zhong, K.S.; et al. Structural deformation characteristics and formation process of Luzhou Block in Sichuan Basin, China. *J. Chengdu Univ. Technol.* **2022**, *49*, 665–673. [CrossRef]
41. Zhang, M.L.; Li, G.Q.; He, J.; Heng, D. Main controlling factors of Ordovician Wufeng-Silurian Longmaxi shale gas enrichment in Tiangongtang structure, southwestern margin of Sichuan Basin. *Lithol. Reserv.* **2022**, *34*, 141–151. [CrossRef]
42. He, D.F.; Lu, R.Q.; Huang, H.Y.; Wang, X.S.; Jiang, H.; Zhang, W.K. Tectonic and geological setting of the earthquake hazards in the Changning shale gas development zone, Sichuan Basin, SW China. *Pet. Explor. Dev.* **2019**, *46*, 993–1003. [CrossRef]
43. Dong, D.Z.; Shi, Z.S.; Sun, S.S.; Guo, C.M.; Zhang, C.C.; Guo, W.; Guan, Q.Z.; Zhang, M.Q.; Jiang, S.; Zhang, L.F.; et al. Factors controlling microfractures in black shale: A case study of Ordovician Wufeng Formation Silurian Longmaxi Formation in Shuanghe Profile, Changning area, Sichuan Basin, SW China. *Pet. Explor. Dev.* **2018**, *45*, 763–774. [CrossRef]
44. Nesbitt, H.W.; Young, G.M. Early Proterozoic climates and plate motions inferred from major element chemistry of lutites. *Nature* **1982**, *299*, 715–717. [CrossRef]
45. Xie, W.Q.; Tan, J.Q.; Wang, W.H.; Schulz, H.M.; Liu, Z.J.; Kang, X.; Wang, Y.; Shahzad, A.; Jan, I.U. Middle Jurassic lacustrine source rocks controlled by an aridification event: A case study in the northern Qaidam Basin (NW China). *Int. J. Coal Geol.* **2021**, *242*, 103779. [CrossRef]
46. Tribovillard, N.; Algeo, T.J.; Baudin, F.; Riboulleau, A. Analysis of marine environmental conditions based on molybdenum-uranium covariation-Applications to Mesozoic paleceanography. *Chem. Geol.* **2012**, *299*, 324–325. [CrossRef]
47. Xie, W.Q.; Jia, J.L.; Miao, C.S.; Wu, Y.J.; Wang, X.M.; Qin, J.Y. Formation and evolution of coal- and oil-bearing source rocks in the Lower Cretaceous Shahai Formation in the Fuxin Basin (NE China): Evidence from organic and inorganic geochemical analyses. *J. Pet. Sci. Eng.* **2021**, *202*, 108544. [CrossRef]
48. Li, Y.F.; Shao, D.Y.; Lv, H.G.; Zhang, Y.; Zhang, X.L.; Zhang, T.W. A relationship between elemental geochemical characteristics and organic matter enrichment in marine shale of Wufeng Formation-Longmaxi Formation, Sichuan Basin. *Acta Pet. Sin.* **2015**, *36*, 1470–1483. [CrossRef]
49. Chang, H.J.; Chu, X.L.; Feng, L.J.; Huang, J.; Zhang, Q.R. Redox Sensitive Trace Elements as Paleoenvironments Proxies. *Geol. Rev.* **2009**, *55*, 91–99. [CrossRef]
50. Wignall, P.B.; Myers, K.J. Interpreting benthic oxygen levels in mudrocks: A new approach. *Geology* **1988**, *16*, 452–455. [CrossRef]
51. Zhang, T.; Wang, L.L.; Liao, H.H.; Zou, M.; Liang, R.; Wang, P.; Su, Z.T. Methods and research progress of Paleo-water depth reconstruction in Sedimentary Basin. *Sediment. Geol. Tethyan Geol.* **2023**, 1–28. [CrossRef]
52. Zhang, Y.Y.; He, Z.L.; Jiang, S.; Gao, B.; Liu, Z.B.; Han, B.; Wang, H. Marine redox stratification during the early Cambrian (ca.529-509Ma) and its control on the development of organic-rich shales in Yangtze Platform. *Geochem. Geophys. Geosystems* **2017**, *18*, 2354–2369. [CrossRef]
53. Goldhammer, T.; Brüchert, V.; Ferdelman, T.G.; Zabel, M. Microbial sequestration of phosphorus in anoxic upwelling sediments. *Nat. Geosci.* **2010**, *3*, 557–561. [CrossRef]
54. Campbell, C.V. Lamina, laminaset, bed and bedset. *Sedimentology* **1967**, *8*, 7–26. [CrossRef]
55. Guo, S.B.; Mao, W.J.; Ma, X. Thermal simulation experiment study of the hydrocarbon generation characteristics of low maturity shale. *Earth Sci. Front.* **2017**, *24*, 365–369. [CrossRef]
56. Huang, L.; Shen, W. Characteristics and controlling factors of the formation of pores of a shale gas reservoir: A case study from Longmaxi Formation of the Upper Yangtze region, China. *Earth Sci. Front.* **2015**, *22*, 374–385. [CrossRef]
57. Gregg, S.J.; Sing, K.S.W. *Adsorption, Surface Area, and Porosity*; Academic Press: New York, NY, USA, 1982. [CrossRef]
58. Thommes, M.; Kaneko, K.; Neimark, A.V.; Olivier, J.P.; Rodriguez-Reinoso, F.; Rouquerol, J.; Sing, K.S.W. Physisorption of gases, with special reference to the evaluation of surface area and pore size distribution (IUPAC Technical Report). *Pure Appl. Chem.* **2015**, *87*, 1051–1069. [CrossRef]
59. Li, Y.Z.; Wang, X.Z.; Wu, B.; Li, G.Q.; Wang, D. Sedimentary facies of marine shale gas formations in Southern China: The Lower Silurian Longmaxi Formation in the southern Sichuan Basin. *J. Earth Sci.* **2016**, *27*, 807–822. [CrossRef]
60. Wang, Y.M.; Li, X.J.; Wang, H.; Jiang, S.; Chen, B.; Ma, J.; Dai, B. Developmental characteristics and geological significance of the bentonite in the Upper Ordovician Wufeng-Lower Silurian Longmaxi Formation in eastern Sichuan Basin, SW China. *Pet. Explor. Dev.* **2019**, *46*, 653–665. [CrossRef]
61. Wang, Y.M.; Dong, D.Z.; Li, X.J.; Huang, J.L.; Wang, S.F.; Wu, W. Stratigraphic sequence and sedimentary characteristics of Lower Silurian Longmaxi Formation in the Sichuan Basin and its peripheral areas. *Nat. Gas Ind.* **2015**, *35*, 12–21. [CrossRef]
62. Schierber, J. Experimental testing of the transport-durability of shale lithics and its implications for interpreting the rock record. *Sediment. Geol.* **2016**, *331*, 162–169. [CrossRef]